NIST Series Technical Note
NIST TN 2377

Mechanisms and Modeling of Corrosion Initiation in RC Structures

Mohammad Amin Hariri-Ardebili
Siamak Sattar

This publication is available free of charge from:
https://doi.org/10.6028/NIST.TN.2377

NIST NATIONAL INSTITUTE OF STANDARDS AND TECHNOLOGY
U.S. DEPARTMENT OF COMMERCE

NIST Series Technical Note
NIST TN 2377

Mechanisms and Modeling of Corrosion Initiation in RC Structures

Mohammad Amin Hariri-Ardebili
Siamak Sattar
Materials and Structural Systems Division
Engineering Laboratory

This publication is available free of charge from:
https://doi.org/10.6028/NIST.TN.2377

May 2026

U.S. Department of Commerce
Howard Lutnick, Secretary

National Institute of Standards and Technology
Craig Burkhardt, Acting Under Secretary of Commerce for Standards and Technology and Acting NIST Director

Publication History
Approved by the NIST Editorial Review Board on 2026-05-20

How to cite this NIST Technical Series Publication:
Mohammad Amin Hariri-Ardebili, Siamak Sattar (2026) Mechanisms and Modeling of Corrosion Initiation in RC Structures. (National Institute of Standards and Technology, Gaithersburg, MD), NIST Technical Note (TN) NIST TN 2377. https://doi.org/10.6028/NIST.TN.2377

NIST Author ORCID iDs
Mohammad Amin Hariri-Ardebili: 0000-0001-6772-1468
Siamak Sattar: 0000-0003-1096-7015

Abstract

Corrosion of reinforcing steel is a leading cause of degradation and loss of functionality in reinforced concrete infrastructure. This report focuses on the initiation stage of corrosion in steel reinforcement, with emphasis on physics-based and computationally efficient models suitable for engineering service life assessment. After reviewing the materials science and electrochemical fundamentals of steel in concrete, the report describes mechanistic pathways to depassivation under carbonation, chloride ingress, and their combined action, including the role of macrocell and microcell corrosion and the nature of corrosion products. Transport models for moisture, chlorides, carbon dioxide, and multiple ionic species are presented, ranging from classical Fickian formulations to fully coupled multi-physics partial differential equation systems. Threshold-based and time-to-initiation models are then discussed, highlighting the transition from simple scalar criteria to multivariate and mechanistic depassivation concepts. The report further summarizes experimental and monitoring techniques needed for parameter identification and validation, and outlines how uncertainties in material, environmental, and model parameters affect predictions of initiation time. Finally, key scientific and modeling gaps are identified, together with a research roadmap that emphasizes improved characterization of the steel–concrete interface, realistic environmental boundary conditions, and integration of corrosion initiation models into broader multi-mechanism aging and structural reliability frameworks.

Keywords

Corrosion; Corrosion initiation; Deterioration; Chloride ingress; Carbonation; Service life assessment; Reinforced concrete; Steel reinforcement; Concrete.

Table of Contents

1. Introduction 1
   1.1. Objectives and Research Questions 4
2. Fundamentals of Corrosion of Steel in Concrete 5
   2.1. Constituents and Microstructure of Cementitious Materials 6
      2.1.1. Hydraulic binders and hydration products 6
      2.1.2. Aggregates and interfacial transition zones 7
      2.1.3. Pore structure, connectivity, and transport-relevant features 9
   2.2. Carbon Steel Reinforcement and Surface Conditions 11
   2.3. Steel–Concrete Interface and Passive Film 12
   2.4. Electrochemical Basics: Thermodynamics and Kinetics 14
   2.5. Concept of Service Life: Initiation and Propagation 16
3. Mechanisms of Depassivation and Corrosion Initiation 17
   3.1. Carbonation-Induced Depassivation 17
   3.2. Chloride-Induced Depassivation 18
   3.3. Combined Carbonation and Chloride Effects 19
   3.4. Macrocell and Microcell Corrosion; Uniform vs. Localized Attack 19
   3.5. Nature, Volume, and Distribution of Corrosion Products 20
   3.6. Corrosion-induced cracking and time-to-cracking models 21
      3.6.1. Empirical models 22
      3.6.2. Analytical models 23
4. Transport of Aggressive Agents and Moisture in Concrete 24
   4.1. Pore Structure, Moisture States, and Degree of Saturation 24
   4.2. Governing Concepts for Moisture Transport 26
   4.3. Chloride Transport: Diffusion, Migration, Convection, and Binding 27
   4.4. Carbonation Modeling and CO_2 Transport 29
   4.5. Coupled Moisture, Heat, and Multi-Ion Transport 31
   4.6. Influence of Mix Design, SCMs, and Concrete Type 32
   4.7. Environmental Exposure Scenarios and Boundary Conditions 33
5. Deterministic Models for Corrosion Initiation 34
   5.1. Threshold-Based Concepts for Depassivation 34

5.1.1. Critical chloride content 34
5.1.2. Carbonation depth and critical pH 36
5.1.3. Limitations of scalar thresholds 36
5.2. Time-to-Initiation Models under Chloride Exposure 37
5.2.1. Closed-form Fickian solutions 37
5.2.2. Incorporating aging, binding, and moisture dependence 38
5.2.3. Convection and non-Fickian effects 39
5.2.4. Existing service life models 39
5.3. Time-to-Initiation Models under Carbonation 40
5.3.1. Empirical $\sqrt{t}$-based models 40
5.3.2. PDE-based carbonation models 40
5.3.3. Moisture and exposure dependence 41
5.4. Multivariate and Mechanistic Criteria 41
5.5. Uniform vs. Localized Initiation and Representative Volume Elements . . . 42
6. Multiphysics PDE Frameworks and Numerical Implementation 44
6.1. Governing Equations for Coupled Transport and Corrosion 44
6.1.1. Moisture and heat 44
6.1.2. Chloride transport with binding 45
6.1.3. CO_2 transport and carbonation 46
6.1.4. Multi-ion transport 47
6.1.5. Corrosion current and metal loss (Faraday's law) 47
6.2. Boundary and Initial Conditions for Realistic Exposures 47
6.2.1. Initial conditions 47
6.2.2. Dirichlet boundary conditions 48
6.2.3. Neumann and Robin (flux/convective) boundary conditions 48
6.2.4. Exposure scenarios 48
6.3. Spatial and Temporal Discretization 49
6.3.1. Semi-discrete form 49
6.3.2. Finite differences and finite volumes 49
6.3.3. Time integration 49
7. Experimental and Monitoring Data for Model Calibration 49

7.1. Laboratory Characterization of Transport Properties 50
7.1.1. Diffusion and migration tests. 50
7.1.2. Sorptivity and capillary suction 50
7.1.3. Permeability and gas transport 51
7.1.4. Chloride binding tests 51
7.2. Field Exposure Sites and Chloride/Carbonation Profiles 51
7.2.1. Chloride profiles in field-exposed elements 51
7.2.2. Carbonation depths and pH indicators 51
7.2.3. Thermogravimetric and microstructural analyses 52
7.3. Electrochemical and Electrical Monitoring Techniques 52
7.3.1. Half-cell potential mapping 52
7.3.2. Concrete resistivity 52
7.3.3. Polarization resistance and Stern–Geary relation 53
7.3.4. Impedance spectroscopy and advanced methods 53
7.4. Accelerated Corrosion and Transport Tests 53
7.4.1. Impressed-current corrosion tests 53
7.4.2. Accelerated carbonation in CO_2 chambers 54
7.4.3. Temperature and humidity acceleration 54
7.5. From Measurements to Model Parameters 54
7.5.1. Curve fitting and single-test identification 54
7.5.2. Multi-test and multi-objective calibration 54
7.5.3. Hybrid physics–data approaches 55
8. Uncertainty, Variability, and Reliability 55
8.1. Sources and Types of Uncertainty in Initiation Models 55
8.2. Role of Corrosion Initiation Models in Service-Life Assessment 56
8.2.1. Durability limit states 56
8.2.2. Role of corrosion initiation models in code calibration 57
9. Summary 57
9.1. Key Scientific and Modeling Gaps 57
9.2. Data and Calibration Challenges 59
9.3. Integration with Structural Analysis and Multi-Mechanism Aging 60

References 62

List of Tables

List of Figures

Fig. 1. Conceptual process of corrosion development in reinforcement; adapted from [1]. 1
Fig. 2. Severe corrosion damage in an abandoned steel-reinforced concrete structure on McAbee Beach in Northern California; adapted from [2]. 2
Fig. 3. Schematic illustration of the service life of RC structures with corrosion deterioration, adapted from Tuutti's diagram [3] and its extension in [4, 5]. 3
Fig. 4. Schematic illustration of two alternative chloride transport pathways (A and B) through the cement paste between coarse aggregates, highlighting how aggregate-induced tortuosity and differences in path length lead to spatial variability of chloride concentration at a given cover depth; adapted from [6]. 8
Fig. 5. A conceptual illustration of spatial variability in corrosion susceptibility along a reinforcing bar, highlighting how local heterogeneities in the steel and steel–concrete interface produce non-uniform critical chloride contents and lead to corrosion initiation at the weakest locations; adapted from [3]. 9
Fig. 6. Simplified Pourbaix (potential–pH) diagram for the iron-water system without chloride, indicating domains of immunity, active corrosion, and passivity for iron. Adapted conceptually from [7]. 15
Fig. 7. Cumulative probability of corrosion initiation versus chloride content from selected laboratory and field datasets, together with a code-based distribution; adapted from [8, 9]. 36
Fig. 8. Closed-form Fickian chloride ingress for a semi-infinite cover. 38

Author Contributions

Mohammad Amin Hariri-Ardebili: Conceptualization, Methodology, Data curation, Writing-Original draft preparation, Visualization, Investigation, Supervision, Writing- Reviewing and Editing; **Siamak Sattar**: Conceptualization, Methodology, Writing- Reviewing and Editing, Investigation.

Acknowledgments

The authors gratefully acknowledge reviewers Dr. Kenneth Snyder, Dr. Patrick Dixon, Dr. Mohammad Houshmand, and Dr. Terri McAllister, National Institute of Standards and Technology (NIST), for their careful review of this report and for providing constructive comments and suggestions that improved the clarity, technical accuracy, and overall quality of the final document. The authors also thank Dr. Dustin Cook, NIST, for providing the cover image.

1. Introduction

Reinforced concrete (RC) is the dominant structural material for bridges, buildings, water-retaining structures, and marine and transportation infrastructure. Its apparent robustness, low material cost, and familiarity in design practice stand in sharp contrast to the vulnerability of embedded steel reinforcement to corrosion. When passivity is lost and corrosion initiates, the resulting loss of steel cross-sectional area, accumulation of corrosion products, cracking and spalling of cover concrete, and loss of bond between the steel and concrete can compromise both serviceability and safety [10] (see Figure 1). At the scale of national infrastructure portfolios, corrosion translates into a substantial economic and environmental burden, with recurring repair and replacement activities contributing significantly to life-cycle costs and embodied carbon.

Fig. 1. Conceptual process of corrosion development in reinforcement; adapted from [1].

Among the various deterioration mechanisms affecting RC, corrosion of reinforcing steel triggered by chloride ingress and/or carbonation is widely recognized as the leading cause of premature degradation in aggressive environments such as marine structures, de-icing salt–exposed bridges, parking structures, and coastal buildings (see Figure 2). In this report, *durability* refers to the ability of a reinforced concrete component or structure to resist environmental and material degradation mechanisms and to maintain its intended functionality over a specified service-life period. This definition connects the materials perspective, which emphasizes transport, chemical reactions, and microstructural change, with the structural-engineering perspective, which emphasizes serviceability, safety, functionality, and maintenance of performance. In aggressive exposure environments, the durability limit state associated with depassivation and subsequent corrosion may govern design or assessment decisions, rather than traditional strength limit states.

Because corrosion initiation is commonly evaluated over multi-decade assessment periods, durability design and service life assessment require credible, physics-based prediction tools that can extrapolate from limited laboratory or field observations to long-term performance under variable exposure conditions. In this report, the term *service life* refers to the time over which a reinforced concrete component or structure satisfies a specified durability or performance criterion.

Conceptually, durability design and assessment of RC structures are often framed in terms of a service life model that separates a predominantly transport-controlled initiation phase

Fig. 2. Severe corrosion damage in an abandoned steel-reinforced concrete structure on McAbee Beach in Northern California; adapted from [2].

from a predominantly mechanically controlled propagation phase. In the classical representation [11], aggressive species (chlorides, carbon dioxide, moisture) are transported through the porous concrete cover until a depassivation condition is reached at the steel surface; beyond this point, corrosion products accumulate, cracks form and propagate, and the structural performance gradually degrades. Figure 3 shows this process conceptually. This conceptual split has been embedded in service life design methodologies and codes, in which the prediction of time-to-initiation serves as a first approximation to durability performance and informs cover requirements, concrete quality, and mitigation measures.

Over the past decades, a substantial body of work has been devoted to modeling both transport and corrosion in concrete, ranging from simplified analytical solutions of Fickian diffusion to fully coupled multi-species, multi-phase transport models combined with electrochemical descriptions of steel corrosion. Monographs, book chapters, and review papers now provide comprehensive summaries of the underlying electrochemistry, transport phenomena, and practical prevention and protection strategies [12, 13]. At the same time, recent critical reviews have highlighted that, despite this rich literature, significant epistemic uncertainties remain in how corrosion is initiated and propagated in real structures subjected to non-ideal exposure histories, complex steel–concrete interfaces, and spatially heterogeneous material properties [4].

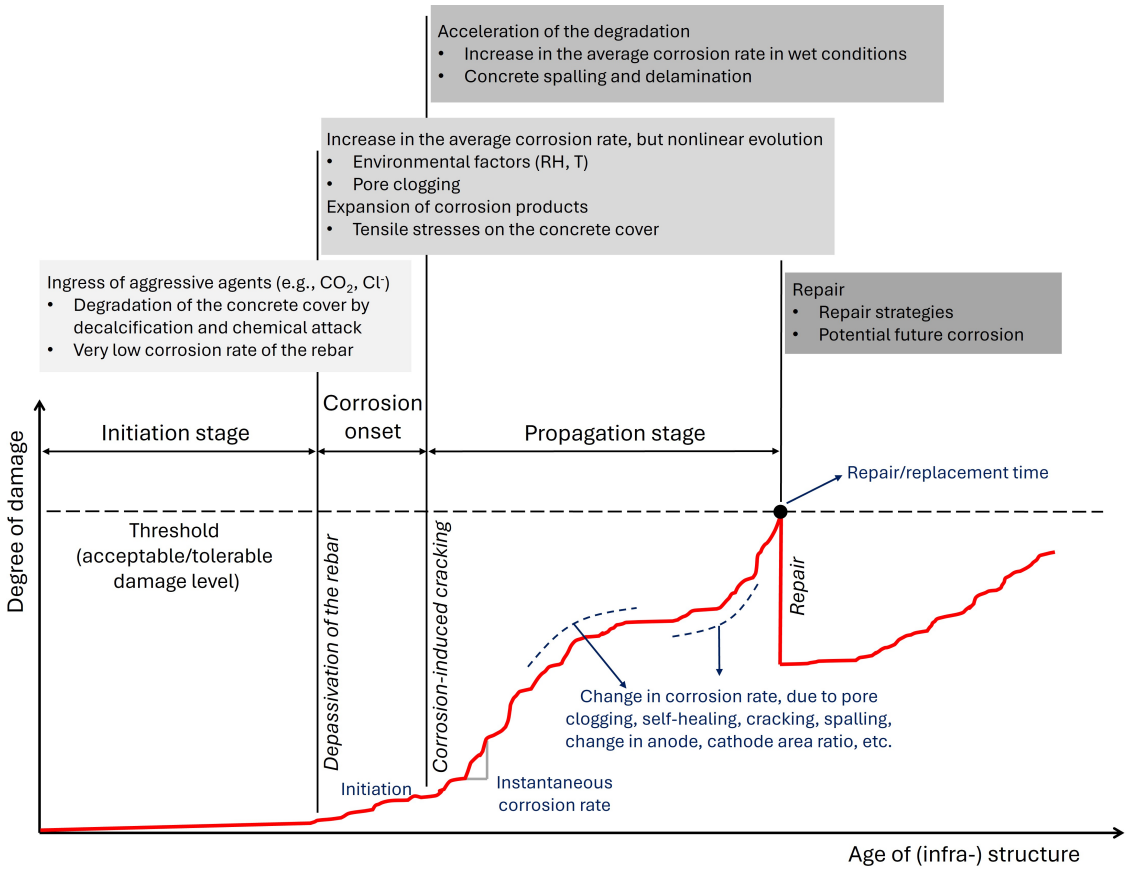

Fig. 3. Schematic illustration of the service life of RC structures with corrosion deterioration, adapted from Tuutti's diagram [3] and its extension in [4, 5].

A central theme emerging from recent work is that the traditional picture of a sharply defined "critical chloride content" or discrete depassivation event is, at best, an engineering idealization. Experimental evidence suggests that steel corrosion in concrete is a continuous process, influenced by local steel surface condition, concrete microstructure, moisture and oxygen availability, the evolving chemistry of the pore solution, and the nature of the exposure environment. In particular, multicomponent ionic exposures such as seawater differ from deicing salt exposures in chemical composition, and therefore in the way species are transported and interact within reactive porous materials such as concrete. Rather than two cleanly separated stages, initiation and propagation overlap in time and space, with low-level corrosion activity occurring well before any conventional threshold is reached and with significant variability between nominally identical specimens. For service-life modeling, this implies that transport and electrochemical processes should be treated in an integrated manner, and that models need to be sensitive to both spatial variability and temporal evolution of environmental actions.

In parallel, there is increasing recognition that corrosion modeling must be embedded

within a broader performance-based and probabilistic framework. Durability design provisions in contemporary model codes explicitly call for the quantification of both variability and uncertainty in material parameters, exposure conditions, and model forms. For high-consequence and/or long-life structures, deterministic predictions based on a single set of input parameters are no longer sufficient; instead, the focus shifts to distributions of time-to-initiation, reliability indices for durability limit states, and optimization of inspection and intervention strategies. Achieving this requires computationally efficient models that retain the essential physics while remaining tractable for large parameter studies, sensitivity analysis, and coupling to structural reliability tools.

The present report responds to these needs by focusing on the *physics-based modeling of transport and corrosion initiation* in RC, at the material and member scale. The emphasis is on mechanistic descriptions of moisture, heat, and multi-ion transport, coupled to electrochemical concepts of passivation and depassivation, formulated in a way that is suitable for numerical implementation (e.g., finite element or finite volume methods). Mechanical damage, cracking, bond degradation, and system-level structural reliability are recognized as critical components of the overall corrosion problem but are treated in companion reports. Here, they appear primarily as context and motivation, and as constraints on the level of detail and accuracy required from initiation models.

1.1. Objectives and Research Questions

The overarching objective of this report is to assemble and consolidate a physics-based framework for modeling corrosion initiation in reinforced concrete structures, with particular emphasis on transport processes and depassivation criteria that are amenable to numerical implementation and subsequent probabilistic analysis. Within this broad aim, several specific objectives and research questions can be identified.

First, the report seeks to formalize how environmental actions and material properties jointly drive passivation and depassivation at the steel surface. This involves clarifying the roles of chloride ingress, carbonation, moisture and oxygen transport, temperature fluctuations, pore solution chemistry, and rebar surface condition, and describing how they interact at the steel–concrete interface to govern the formation, stability, and breakdown of the passive film. A central question is how best to represent this interaction at the level of engineering models: through simple threshold criteria, through multivariate passivation/depassivation conditions, or through explicit, time-dependent corrosion rate formulations.

Second, the report aims to formulate coupled transport–electrochemical models within a unified multi-physics partial differential equation framework. This entails specifying mass and energy balance equations for the relevant phases and species, selecting appropriate constitutive relations for transport and reaction terms, and defining boundary and initial conditions representative of realistic exposure scenarios. A key question is the level of mechanistic detail required to capture the dominant features of initiation under typical field conditions, and the conditions under which simplified or reduced-order models can be jus-

tified for engineering applications.

Third, the report addresses the challenge of parameterization and calibration of initiation models. Transport and electrochemical parameters exhibit substantial variability across concretes with different binders, curing regimes, and exposure histories, and many parameters are not directly measurable. A useful strategy is therefore to focus on measurable representative descriptors of multiple interacting factors, together with their associated uncertainty bounds, rather than only on isolated model parameters. Accordingly, we ask how laboratory tests, long-term field data, and electrochemical measurements can be most effectively combined to identify model parameters and constrain predictions of time-to-initiation. Particular attention is given to the steel–concrete interface, critical chloride concepts, local heterogeneities, and pore solution chemistry as a representative descriptor that may support calibration in both laboratory and field settings.

Fourth, the report seeks to clarify how initiation models can be embedded within probabilistic frameworks for durability and service-life assessment. While a full reliability treatment is outside the scope of this document, it is essential to understand which input parameters and model features most strongly affect the distribution of initiation times. This leads to questions about sensitivity, dominant uncertainty sources, and the design of computationally efficient models that remain compatible with Monte Carlo or surrogate-based approaches at later stages.

Finally, the report aims to identify key modeling considerations relevant to the formulation, calibration, and interpretation of corrosion-initiation models. By discussing governing mechanisms, representative exposure conditions, and relevant measurements, the report provides a technical basis for future comparison of modeling approaches and for eventual code development.

2. Fundamentals of Corrosion of Steel in Concrete

Corrosion of reinforcing steel in concrete takes place in a highly complex, multi-scale environment where solid phases, pore solution, and gaseous phases coexist and interact. At the smallest scales, the microstructure of the hydrated binder (generally cement based) controls the composition and transport properties of the pore solution; at intermediate scales, aggregates and interfacial transition zones (ITZs) modulate tortuosity and connectivity of transport pathways; and at member scale, cracking and construction details govern exposure and moisture exchange with the environment. A mechanistic understanding of corrosion in reinforced concrete therefore requires, as a foundation, a clear picture of the relevant constituents of cementitious materials and their microstructure, with emphasis on features that influence ion transport, moisture migration, and the stability of the passive film on steel [14–17].

From the corrosion perspective, several material characteristics are particularly important. The solid phases formed during cement hydration (primarily calcium silicate hydrate, C–

S–H, and portlandite) determine both the alkalinity and buffering capacity of the pore solution, which in turn control the initial passivation of steel and its resistance to carbonation-induced depassivation [14, 18]. The pore system — including gel pores, capillary pores, air voids, and microcracks — controls the effective diffusivity and permeability for chlorides, carbon dioxide, oxygen, and moisture [17, 19]. Supplementary cementitious materials (SCMs) and alternative binders modify this microstructure and pore solution chemistry, often refining pore sizes and altering chloride chemical binding capacity, but also changing carbonation resistance [20]. At larger scales, the presence of aggregates and the associated ITZs introduce pronounced heterogeneity in porosity and transport properties, leading to spatial variability in exposure conditions at the steel surface [6, 21].

The purpose of this section is not to provide an exhaustive materials science treatment of cement and concrete, but rather to collect those concepts and micro-structural features that are essential for the formulation of transport and initiation models used later in the report. The focus is on (i) the main hydration products and their role in defining pore solution chemistry and sorption behaviour; (ii) the pore structure and its dependence on mixture design, curing, and environmental exposure; and (iii) meso-scale heterogeneities such as ITZs and steel–concrete interfaces that are particularly relevant for localized corrosion and spatial variability in depassivation.

2.1. Constituents and Microstructure of Cementitious Materials

2.1.1. Hydraulic binders and hydration products

Conventional reinforced concrete is most commonly based on ordinary Portland cement (OPC) or blended cements, optionally supplemented by mineral admixtures such as fly ash, slag, silica fume, or calcined clays. Clinker production yields four main anhydrous phases (alite C_3S, belite C_2S, aluminate C_3A, and ferrite C_4AF), which react with water to form a suite of hydration products [13–15]. At a simplified level, the main silicate hydration reactions can be represented as

$$2\,C_3S + 6\,H \;\rightarrow\; C_3S_2H_3 + 3\,CH, \tag{1}$$

$$2\,C_2S + 4\,H \;\rightarrow\; C_3S_2H_3 + CH, \tag{2}$$

where C, S, A, F, and H are the cement chemistry shorthands for CaO, SiO_2, Al_2O_3, Fe_2O_3, and H_2O, respectively; $C_3S_2H_3$ denotes C–S–H, and CH denotes portlandite [14]. Although the actual composition of C–S–H is variable and hydration products form through more complex reaction pathways, Eqs. (1)–(2) capture the essential features: formation of a low-solubility binding phase (C–S–H) and an alkaline reservoir (portlandite).

After sufficient curing, C–S–H typically accounts for about 50–60% of the hydrated cement paste by mass and provides most of its mechanical cohesion [22]. Its nanostructure consists of lamellar silicate chains with interlayer calcium and water; variations in Ca/Si ratio, degree of polymerisation, and water content control its density, specific surface area, and

sorption behavior [18]. Portlandite, while mechanically less important, plays a crucial role as an alkaline reservoir: its dissolution governs pH buffering during leaching and carbonation, and its presence or depletion has direct implications for the stability of the passive film on steel [23]. Aluminate-bearing hydrates, including ettringite and aluminate–ferrite monosubstituted (AFm) phases, contribute to the chemical binding of sulfate and, particularly in concretes containing supplementary cementitious materials (SCMs), can also influence chloride binding and the evolution of pore solution chemistry [24].

The incorporation of SCMs modifies both hydration kinetics and the assemblage of hydrates. Pozzolanic additions such as fly ash or silica fume consume portlandite and produce additional C–S–H with lower Ca/Si ratios, which tends to refine the pore structure and reduce permeability, but also affects carbonation rate and chloride binding capacity [15, 20]. Latent hydraulic slag and limestone additions introduce further complexity, as they participate in additional hydration and carboaluminate-forming reactions. From the standpoint of corrosion modeling, these modifications must eventually be reflected in different effective transport coefficients and in altered chemical boundary conditions at the steel surface.

2.1.2. Aggregates and interfacial transition zones

Aggregates occupy roughly 60–80% of the concrete volume and are often idealized as inert, impermeable inclusions. In reality, their presence has two competing effects on transport and durability: they increase the tortuosity of the pore network (generally beneficial for resistance to ingress), but they also introduce interfacial transition zones (ITZs) between aggregate and paste, which are typically more porous and less homogeneous than the bulk paste [15, 21]. The ITZ arises due to wall effects, bleeding, and packing constraints during casting and early hydration, leading to higher local water-to-cement ratios, preferential orientation of hydrates, and sometimes micro-cracking.

Experimental studies using backscattered electron imaging, microtomography, and image analysis have characterised ITZ thicknesses on the order of 20–50 μm and documented higher capillary porosity and different hydrate assemblages relative to the bulk paste [25–27]. From the transport perspective, the ITZ can form a relatively conductive shell around aggregates and, when sufficiently connected, can increase the effective diffusivity or conductivity of concrete relative to an aggregate–paste system with no explicit ITZ. This effect has been studied in detail by Bentz and Garboczi, which showed that transport depends not only on the contrast between ITZ and bulk paste properties but also on the volume fraction and percolation of the ITZ network [28, 29]. At the meso-scale, it is therefore natural to represent concrete as a composite of aggregates, ITZ, and bulk paste, each with its own transport properties; several numerical frameworks for moisture and ion transport explicitly adopt this decomposition [30, 31].

At the meso-scale, the chloride front does not advance as a smooth plane but via a collection of tortuous pathways through the cement paste between coarse aggregates. Figure 4 schematically illustrates two idealized transport paths (A and B): a longer, more

tortuous route and a shorter, more direct route with higher transport capacity through the paste. When the cover depth is of the same order as the maximum aggregate size, such differences in path length and connectivity generate pronounced spatial variability in chloride concentration at a given depth, even under nominally homogeneous exposure. This schematic supports experimental evidence that aggregate geometry and pore tortuosity are primary drivers of scatter in chloride profiles, often overshadowing the more modest effects of binder type or water-to-binder (w/b) ratio.

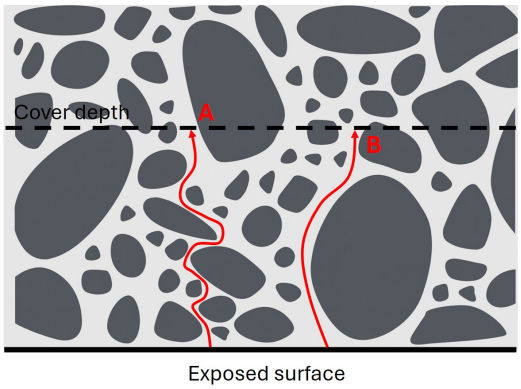

Fig. 4. Schematic illustration of two alternative chloride transport pathways (A and B) through the cement paste between coarse aggregates, highlighting how aggregate-induced tortuosity and differences in path length lead to spatial variability of chloride concentration at a given cover depth; adapted from [6].

In addition to aggregate-related ITZs, the steel–concrete interface (SCI) itself is a critical micro-structural region. Casting and bleeding around reinforcement can lead to preferential porosity, micro-voids, and heterogeneity in pore solution composition in the immediate vicinity of the bar, which in turn influence depassivation and spatial variability of corrosion initiation [4, 27]. Although the SCI will be discussed in more detail in a later subsection, it is worth noting already here that transport and electrochemical processes at the steel surface are strongly conditioned by meso-scale microstructure and heterogeneity around the bars.

Figure 5 shows the variability of corrosion along a component. It schematically illustrates how both metallurgical heterogeneities in the steel (e.g., inclusions, surface roughness, oxide-layer defects) and spatial variations in the steel–concrete interface and ITZ (e.g., porosity, local chemistry, micro-cracks, air voids) create a highly non-uniform resistance to corrosion along the bar. As a result, each point on the reinforcement has its own local critical chloride content, and corrosion will initiate at the weakest point with the lowest threshold once a nearly uniform chloride front reaches the steel. The critical chloride content measured in a laboratory specimen is therefore essentially the minimum local value sampled along the exposed length, making it an extreme-value (weakest-link) quantity [8]. Consequently, the apparent critical chloride content depends on specimen size: longer bars have a higher chance of containing weak points and thus tend to exhibit lower measured thresholds and different scatter than sets of shorter specimens.

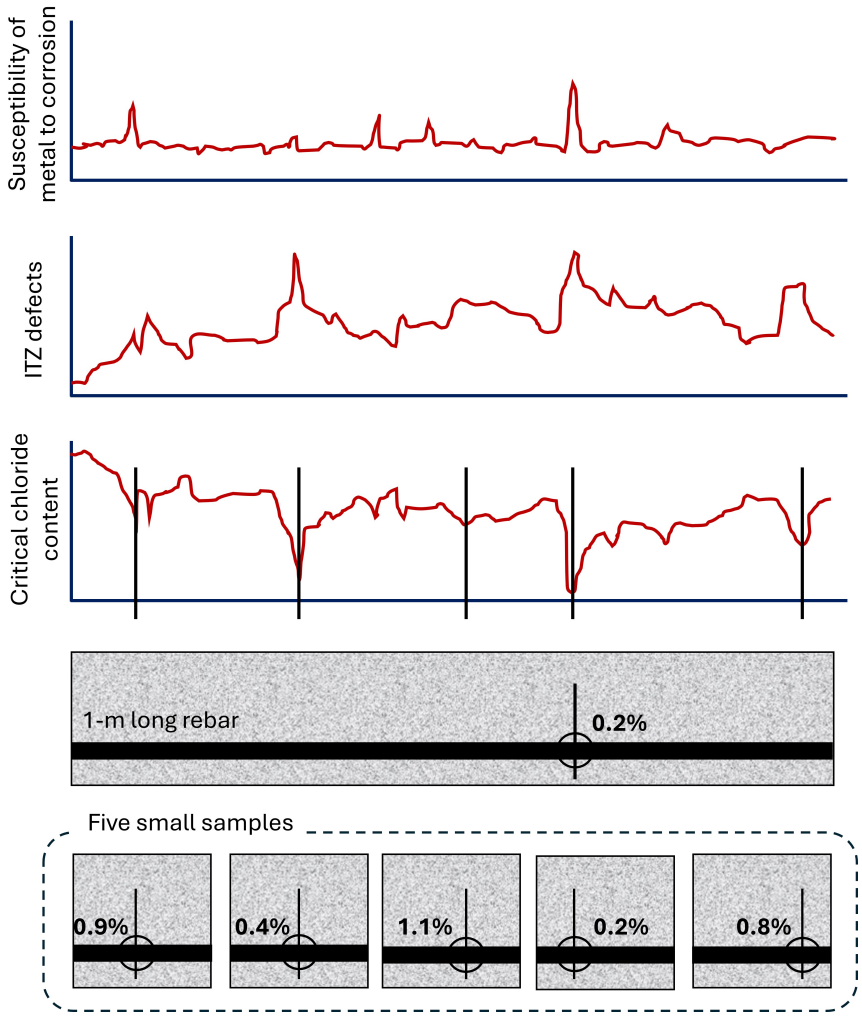

Fig. 5. A conceptual illustration of spatial variability in corrosion susceptibility along a reinforcing bar, highlighting how local heterogeneities in the steel and steel–concrete interface produce non-uniform critical chloride contents and lead to corrosion initiation at the weakest locations; adapted from [3].

2.1.3. Pore structure, connectivity, and transport-relevant features

At the scale of hydrated cement paste, the microstructure can be viewed as a solid skeleton of hydrates and unreacted clinker, interspersed with a connected pore network ranging from nanometer-scale gel pores within C–S–H to micrometer-scale capillary pores and larger voids. A classical distinction is made between gel pores ($\lesssim$ 10 nm), small capillary pores ($\sim$ 10–100 nm), and larger capillary or air voids ($\gtrsim$ 100 nm), although in practice the pore size distribution is continuous [15, 16]. Gel pores are predominantly water-filled under normal exposure conditions and contribute to sorption but relatively little to long-range transport; capillary pores, by contrast, largely control effective diffusivity and permeability

for ionic and gaseous species [17, 19].

Two simple descriptors that will recur in later sections are the (total) porosity ϕ_p and the degree of saturation S:

$$\phi_p = \frac{V_p}{V_{tot}}, \tag{3}$$

$$S = \frac{V_w}{V_p}, \tag{4}$$

where V_p is the pore volume, V_w the volume of pore water, and V_{tot} the total volume of the material element. The volumetric water content W is then $W = S\phi_p$. For saturated porous materials, a useful transport descriptor is the formation factor F_f, defined as the ratio of the electrical conductivity of the pore solution to that of the material saturated with the same pore solution. This quantity provides a compact measure of the effects of pore connectivity and tortuosity on transport. For dilute electrolytes in an inert saturated microstructure, the effective diffusion coefficient may then be written as

$$D_{eff} = \frac{D_0}{F_f}, \tag{5}$$

where D_0 is the self-diffusion coefficient in the pore solution.

Under saturated conditions, it is useful to distinguish between the self-diffusion coefficient in the pore solution, the microstructural diffusion coefficient that reflects the geometry of the porous network, and the apparent diffusion coefficient inferred at the material scale. In nonreactive porous systems, the long-time diffusive response can be characterized primarily by porosity and formation factor, while the effects of ionic speciation enter through the pore-solution diffusivity [32, 33]. In cementitious materials, however, this picture is further complicated by chemical binding, buffering, and other reactions within the pore structure. For engineering applications under partially saturated conditions, these effects are often represented in lumped form through an effective or apparent diffusion coefficient with additional dependence on saturation, for example

$$D_{app}(S) = D_{sat} S^m, \tag{6}$$

where D_{sat} denotes the saturated apparent diffusion coefficient and m is an exponent reflecting the connectivity and tortuosity of the liquid phase [17, 24, 32, 33].

The volume fraction, size distribution, and connectivity of capillary pores depend strongly on w/b ratio, degree of hydration, and curing conditions. Higher water-to-cement ratios leave more unfilled capillary space and result in larger and more connected pores, increasing transport rates. Continued hydration and pozzolanic reactions with SCMs gradually refine the pore structure, reducing pore sizes and connectivity and thereby lowering permeability and diffusion coefficients over time [34, 35]. Environmental actions such as leaching or carbonation can in turn modify the microstructure: decalcification of C–S–H

and dissolution of portlandite alter porosity and pore connectivity, with implications for both transport and pore solution chemistry [36].

From a modeling standpoint, this complex pore system is often upscaled into effective continuum parameters such as moisture-dependent diffusivity, permeability, and sorption isotherms [37–39]. Multi-scale studies and image-based simulations have demonstrated that these effective properties are sensitive not only to average porosity but also to the topology of the pore network, including percolation thresholds and preferential pathways [19, 40]. For corrosion initiation, the key outcome is that the rate at which chlorides, carbon dioxide, and oxygen reach the steel surface is governed by a combination of pore size distribution, connectivity, degree of saturation, and meso-scale heterogeneity; these features must therefore be appropriately represented, either explicitly or implicitly, in transport models.

Finally, the microstructure is not static over the service life. Hydration and SCM reactions, drying and wetting cycles, carbonation, and other degradation mechanisms can all induce time-dependent changes in pore structure and pore solution composition. For physics-based corrosion initiation models, it is often necessary to decide whether to treat microstructure and associated transport properties as fixed (e.g., at a representative age) or to incorporate their evolution explicitly. The present report will mostly adopt the former view for clarity, while noting that time-dependent micro-structural evolution is an important frontier for future modeling efforts, particularly in long-term service-life assessments and coupled chemo-mechanical simulations.

2.2. Carbon Steel Reinforcement and Surface Conditions

Reinforcing bars used in conventional concrete construction are typically low-carbon steels with carbon contents in the range of 0.15–0.30 wt. %, with additions of Mn, Si, and sometimes micro-alloying elements such as V, Nb, or Cr to control strength and toughness [10, 41]. At the metallurgical scale, the as-rolled microstructure is usually a mixture of ferrite and pearlite, with grain size, phase fraction, and banding patterns depending on the steel grade and thermo-mechanical processing. Variations in ferrite/pearlite morphology, segregation bands, and inclusion populations introduce small galvanic cells within the bar cross-section, leading to differences in local anodic and cathodic behavior that can be relevant for pit initiation and early-stage corrosion kinetics [42, 43].

During hot rolling, a complex iron-oxide scale forms on the bar surface. This “mill scale” typically consists of layered wüstite (FeO), magnetite (Fe_3O_4), and hematite (Fe_2O_3), often with cracks and detachments due to thermal cycling and deformation. Subsequent bending, cutting, storage, and handling partially remove this scale and may generate additional surface defects. When the bar is eventually embedded in fresh concrete, residues of mill scale and pre-existing rust patches coexist with bare steel areas. In the highly alkaline pore solution ($pH \gtrsim 13$), the mill scale is thermodynamically unstable; it gradually dissolves or transforms while a new passive film nucleates and grows on the underlying steel [10]. The

spatially heterogeneous transition from as-rolled surface to mature passive film contributes to variability in the local electrochemical conditions at early ages.

Surface condition before casting is further modified by atmospheric exposure. Bars are often stored outdoors, leading to wet–dry cycling, deposition of chlorides and other contaminants, and formation of rust layers of variable thickness and composition. Experimental studies indicate that light, adherent rust may increase mechanical bond and does not necessarily impair corrosion performance, whereas thick, flaky rust and contamination by de-icing salts or marine aerosols can create local chloride reservoirs at the steel–concrete interface [41]. Such pre-rusted spots may act as preferential sites for early depassivation once the surrounding concrete carbonates or additional chlorides arrive.

Non-metallic inclusions, particularly MnS and Al_2O_3-based particles inherited from steelmaking, are another micro-structural feature of interest. In mildly aggressive environments, inclusions can become sites of local acidification (e.g., due to sulfide oxidation) and mechanical weakness, promoting pit nucleation at relatively low chloride concentrations [41]. Modern bar production has reduced the size and frequency of harmful inclusions, but older steels may exhibit higher inclusion contents and stronger banding, which can contribute to scatter in corrosion initiation times between nominally identical bars. Heat treatment and controlled cooling can also alter the gradient of microstructure from the bar surface to its core, changing both mechanical properties and corrosion response [42, 43].

From a modeling standpoint, it is convenient to treat carbon steel reinforcement as an electrically conducting, homogeneous phase with well-defined anodic and cathodic kinetics. However, the underlying metallurgical heterogeneity and surface condition — residual scale, pre-rust, inclusions, and cold-working damage — help explain why measured corrosion rates and pit morphologies exhibit considerable scatter even under nominally uniform exposure.

2.3. Steel–Concrete Interface and Passive Film

The steel–concrete interface (SCI) is not a sharp boundary, but a heterogeneous transition zone where steel, hydrates, pore solution, and voids coexist over tens to hundreds of micrometres [44]. Casting orientation, bleeding, settlement of aggregates, and the presence of formwork or bar chairs all influence how this zone develops. For horizontal members, "top-bar" effects are well documented: bleeding water tends to accumulate beneath the upper reinforcement, leaving higher local porosity, more entrapped air, and sometimes preferential channels aligned along the bar. Around vertically oriented bars, segregation patterns differ, but similar local variations in w/b ratio, ITZ thickness, and micro-cracking are observed [44, 45].

Recent experimental work has used backscattered electron imaging, X-ray micro-tomography, and, more recently, FIB–SEM nano-tomography to characterize the SCI in three dimensions [27]. These studies reveal a complex mosaic of hydrates, capillary pores, and mi-

crovoids adjacent to the steel, with spatially variable connectivity to the bulk pore system. Locally increased porosity and micro-cracking at the SCI can facilitate access of chlorides, carbon dioxide, and oxygen to the bar surface. Conversely, dense regions with good contact and low porosity may delay ingress and prolong passivity. For chloride exposure in particular, the SCI has been shown to exhibit chloride concentrations and moisture conditions that differ significantly from those inferred from conventional powder sampling at a few millimetres distance [44, 45]. Any realistic transport model for corrosion initiation must therefore either resolve or effectively homogenise these interfacial features.

When steel is embedded in fresh concrete, its surface is quickly exposed to an aqueous, highly alkaline pore solution dominated by Na^+, K^+, Ca^{2+}, OH^-, and, depending on binder composition, aluminates and other species. Under such conditions, iron is thermodynamically stable in a passive state over a broad potential range, as can be seen from iron–water Pourbaix diagrams at $pH \approx 13$ [7]. A nanometre-scale passive film forms spontaneously, typically consisting of an inner layer of mixed Fe(II)/Fe(III) oxides (often modeled as Fe_3O_4 or Fe_2O_3-rich) and an outer layer of hydrated Fe(III) oxyhydroxides such as γ-FeOOH, with small amounts of incorporated alloying elements and adsorbed ions [46, 47]. Reported thicknesses of this film on rebars in simulated pore solution are of order 2–10 nm, depending on exposure time, composition, and prehistory.

Electrochemical studies using impedance spectroscopy, Mott–Schottky analysis, and XPS depth profiling have shown that the passive film on rebars behaves as a defective semiconductor, with semiconductive behavior arising from point defects and non-ideal film stoichiometry; the corresponding donor and acceptor densities vary with alloy composition, pore solution chemistry, and the presence of inhibitors [46, 47]. These semiconductive properties are relevant because they govern the distribution of electric field and potential drop across the film and thus influence both the stability of passivity and the susceptibility to local breakdown under chloride attack. For example, films formed in saturated $Ca(OH)_2$ solutions often exhibit lower defect densities and higher charge-transfer resistance than those formed in NaOH solutions at similar pH, reflecting subtle differences in film composition and porosity [47].

At the SCI, the passive film must be understood as part of a coupled system: the local pore structure influences access of aggressive species; the pore solution composition and pH determine film growth and dissolution; and the bar microstructure (e.g., inclusions, banding) provides potential nucleation sites for localized breakdown. The SCI is also the location where mechanical actions (shrinkage, thermal strains, and later corrosion-induced expansion) produce micro-cracks that, in turn, affect mass transport and local electrochemistry [44, 45]. The present report will not attempt to model the SCI at full micro-structural resolution, but will draw on these insights to motivate effective boundary conditions and stochastic representations of spatial variability in depassivation.

2.4. Electrochemical Basics: Thermodynamics and Kinetics

Corrosion of steel in concrete is an electrochemical process involving coupled anodic and cathodic half-reactions, charge transfer across interfaces, and mass transport in the pore solution. At the anodic sites, iron is oxidised according to

$$\mathrm{Fe} \;\rightarrow\; \mathrm{Fe}^{2+} + 2\,\mathrm{e}^{-}, \tag{7}$$

with subsequent hydrolysis and precipitation of hydroxides and oxides. In aerated, alkaline pore solution, the dominant cathodic reaction is the reduction of dissolved oxygen:

$$\mathrm{O_2} + 2\,\mathrm{H_2O} + 4\,\mathrm{e}^{-} \;\rightarrow\; 4\,\mathrm{OH}^{-}. \tag{8}$$

Hydrogen evolution is usually negligible under normal conditions in concrete, but may become relevant locally in severely oxygen-depleted or extremely alkaline environments. The overall corrosion process is controlled by the balance of these anodic and cathodic currents, constrained by charge conservation and, in many cases, by mass-transport limitations of oxygen or reactants [41, 48].

Thermodynamic aspects of corrosion are often visualized using Pourbaix (potential–pH) diagrams, which map domains of immunity, active corrosion, and passivity for a given metal/solution system [7]. For iron in contact with concrete pore solution, the relevant region lies at high pH ($\approx$ 12.5–14) and potentials where Fe is predicted to be covered by a stable oxide/hydroxide film. The Nernst equation,

$$E_{\mathrm{eq}} = E^{\circ} - \frac{RT}{nF} \ln \frac{a_{\mathrm{Red}}}{a_{\mathrm{Ox}}}, \tag{9}$$

links the equilibrium potential E_{eq} of a redox couple to the standard electrode potential E°, the activities a_{Red} and a_{Ox} of reduced and oxidized species, temperature T, electron number n, and Faraday constant F. In principle, Eq. (9) can be used to estimate how changes in pH, chloride activity, or other species shift equilibrium potentials of anodic and cathodic reactions, and thus the location of the system in the Pourbaix diagram [41]. Figure 6 illustrates a simplified Pourbaix diagram for the iron-water system without chloride presence.

Kinetic aspects are commonly described by mixed-potential theory and Butler–Volmer kinetics. For a single electrode reaction, the local current density i as a function of overpotential $\eta = E_{\mathrm{loc}} - E_{\mathrm{eq}}$ is given by

$$i(\eta) \;=\; i_0 \left[\exp\!\left(\frac{\alpha_{\mathrm{a}} F \eta}{RT} \right) - \exp\!\left(-\frac{\alpha_{\mathrm{c}} F \eta}{RT} \right) \right], \tag{10}$$

where i_0 is the exchange current density, E_{loc} is the local electrode potential, and α_{a}, α_{c} are anodic and cathodic charge-transfer coefficients [48]. For sufficiently large overpotentials and when one exponential term dominates, Eq. (10) reduces to the familiar Tafel

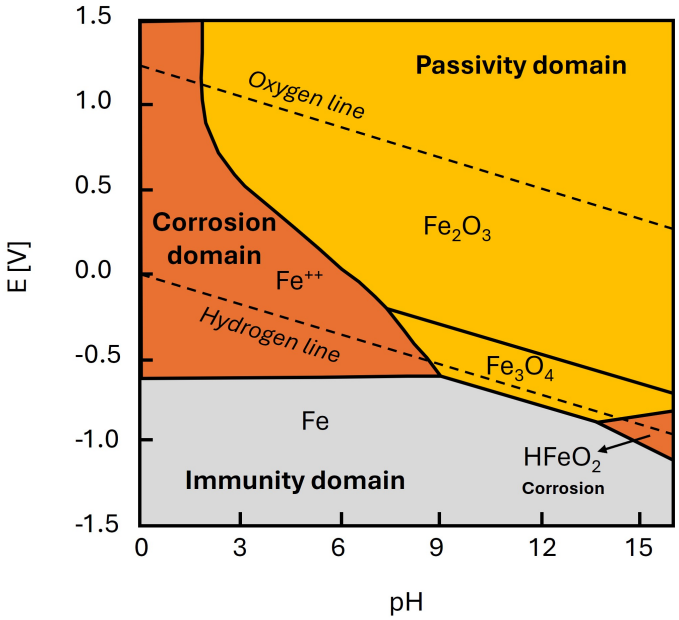

Fig. 6. Simplified Pourbaix (potential–pH) diagram for the iron-water system without chloride, indicating domains of immunity, active corrosion, and passivity for iron. Adapted conceptually from [7].

relationships, which are widely used to interpret polarization curves for steel in concrete environments [10, 41]. Near the corrosion potential E_{corr}, linearization of Eq. (10) leads to relationships between the slope of the potential–current curve (polarization resistance) and the corrosion current density.

In a concrete structure, the measured corrosion potential E_{corr} is the mixed potential at which the net anodic and cathodic currents balance when integrated over all active and passive areas of the reinforcement. Its value is influenced by bar geometry, macrocell formation, and spatial variability in moisture and oxygen availability, as well as by the degree of passivation or depassivation [41]. Oxygen transport through the concrete cover often limits the cathodic reaction, especially in thick or saturated members, introducing an additional coupling between electrochemistry and mass transport. As the passive film breaks down locally (e.g., due to chloride accumulation), small anodic regions with high current density coexist with surrounding passive areas, and the macroscopic response reflects a complex superposition of local kinetics and ohmic drops in the concrete.

For the purposes of this report, the key electrochemical quantities are (i) the corrosion potential E_{corr}, (ii) the corrosion current density i_{corr} associated with uniform or localized dissolution, and (iii) parameters in Eqs. (9)–(10) that depend on pH, ionic composition, and passive-film properties.

2.5. Concept of Service Life: Initiation and Propagation

The service life of reinforced concrete structures subject to corrosion is often conceptualized as the sum of two distinct phases: an initiation period, during which the steel remains passive, and a propagation period, during which active corrosion leads to cracking, spalling, and loss of structural capacity. This framework, introduced in Kyösti Tuutti's seminal work on corrosion of steel in concrete [3], remains the backbone of most modern service life models and codified approaches. In its simplest form, the total service life t_{SL} is written as

$$t_{\mathrm{SL}} \;=\; t_{\mathrm{init}} + t_{\mathrm{prop}}, \tag{11}$$

where t_{init} is controlled by transport of aggressive agents and depassivation, and t_{prop} by corrosion kinetics, cracking evolution, and maintenance strategies.

For chloride-induced corrosion, the initiation phase is often defined as the period required for the chloride concentration at the steel surface, $C(x_{\mathrm{cover}},t)$, to reach a critical threshold C_{crit}:

$$C(x_{\mathrm{cover}},t_{\mathrm{init}}) \;=\; C_{\mathrm{crit}}, \quad \text{or} \quad \frac{C_{\mathrm{tot}}}{m_{\mathrm{cement}}}(x_{\mathrm{cover}},t_{\mathrm{init}}) = C_{\mathrm{crit}}^{\mathrm{mass}}, \tag{12}$$

where x_{cover} is the depth of the reinforcement measured from the exposed concrete surface, and $C_{\mathrm{crit}}^{\mathrm{mass}}$ is a mass-based threshold (e.g., % Cl^- by mass of cement) [22]. The evolution of $C(x,t)$ is governed by coupled diffusion, convection, and binding processes that will be detailed in later sections. The value of C_{crit} itself is not a fixed material constant but a stochastic quantity influenced by bar surface condition, SCI properties, electrochemical environment, and the counter-diffusion of alkalis and chloride ions [41]. For carbonation-induced corrosion, an analogous criterion is often posed in terms of the carbonation front depth $x_{\mathrm{carb}}(t)$ reaching the reinforcement:

$$x_{\mathrm{carb}}(t_{\mathrm{init}}) \;=\; x_{\mathrm{cover}}, \tag{13}$$

typically associated with a drop in pore-solution pH below a level at which the passive film on steel becomes unstable. In practice, additional threshold definitions involving pH, moisture state, and oxygen availability are sometimes used to refine the boundary between initiation and propagation [10, 20].

While the two-phase representation is conceptually clean and convenient for design, it is an idealization. Experimental and field observations show that depassivation is often gradual, with localized breakdown and repassivation events occurring over a range of chloride contents or degrees of carbonation [4]. Likewise, corrosion-induced cracking and rust expansion may begin during what a deterministic model would still classify as the initiation phase, especially in members with thin cover or significant restraint. Recent work has therefore emphasised probabilistic formulations of service life, in which both t_{init} and t_{prop} are random variables influenced by uncertainties in material parameters, exposure histories, and modeling assumptions [4, 41].

3. Mechanisms of Depassivation and Corrosion Initiation

Corrosion of reinforcement in concrete is generally understood as a consequence of loss of passivity of the steel surface in an otherwise highly alkaline, protective pore solution. In reinforced concrete, depassivation is most commonly driven by chloride ingress from marine or de-icing environments, with carbonation playing a significant but usually secondary role in most infrastructure exposures [4, 49]. From a mechanistic viewpoint, both carbonation and chlorides modify the chemical and electrochemical conditions at the steel–concrete interface in ways that destabilize the passive film and enable active anodic dissolution.

This section reviews the key depassivation mechanisms that control the initiation phase of corrosion: (i) carbonation-induced pH reduction; (ii) chloride-induced breakdown of passivity; (iii) combined carbonation–chloride effects; and (iv) the manifestation of these mechanisms as microcell and macrocell corrosion, with uniform vs. localized attack. The emphasis is on chloride-induced depassivation, in line with the dominant deterioration scenario for RC bridges, parking structures, and marine concrete.

3.1. Carbonation-Induced Depassivation

In sound, uncarbonated concrete, the pore solution is highly alkaline (pH $\gtrsim$ 12.5), with $[OH^-]$ on the order of 0.1–1.0 mol/L, which stabilizes a thin, protective iron oxide/hydroxide passive film on the steel surface [50]. Carbonation is initiated when atmospheric CO_2 diffuses into partially saturated concrete, dissolves in pore water, and reacts with portlandite ($Ca(OH)_2$) and, at later stages, with C–S–H and other hydrates:

$$Ca(OH)_2 + CO_2 \rightarrow CaCO_3 + H_2O, \tag{14}$$

$$C-S-H + CO_2 \rightarrow SiO_2\,(gel) + CaCO_3 + H_2O. \tag{15}$$

These reactions consume hydroxide, reduce the buffering capacity, and gradually lower the pore solution pH.

At the structural scale, carbonation is often idealized as a moving front that advances into the cover with an approximate square-root-of-time dependence, as is typical of diffusion-limited systems:

$$x_{\mathrm{carb}}(t) \approx k_{\mathrm{carb}}\sqrt{t}, \tag{16}$$

where x_{carb} is the carbonation depth, t is exposure time, and k_{carb} is an apparent carbonation coefficient that depends on mix design, humidity, temperature, and CO_2 concentration [50]. In reality, however, the carbonation front is neither sharp nor planar: local heterogeneities in pore structure, moisture state, and cracking lead to a diffuse and spatially variable transition zone [51]. This non-uniformity is relevant for depassivation, because the steel–concrete interface may be locally carbonated (and depassivated) even when the bulk carbonation depth, measured on cores or slices, has not yet reached the nominal bar depth.

Depassivation by carbonation is commonly assumed once the carbonation front reaches the steel depth and the local pH drops below a critical value (often taken in the range 9–10),

at which the passive film on carbon steel is no longer thermodynamically stable [50]. In practice, this criterion is strongly modulated by moisture availability and oxygen access; many field observations show that fully saturated, deeply carbonated regions can remain essentially corrosion-free, whereas partially saturated, carbonated zones with good oxygen supply are much more prone to active corrosion [51].

3.2. Chloride-Induced Depassivation

Chloride-induced corrosion is widely recognized as the primary cause of premature deterioration of RC structures exposed to marine environments or de-icing salts [4, 49]. Chlorides may be present as (i) externally applied surface loads (sea spray, tidal immersion, splash, ponding, de-icing brines), or (ii) internally mixed chlorides from contaminated aggregates, mixing water, or admixtures. After ingress into concrete, chlorides are partitioned between a free fraction in the pore solution and a bound fraction associated with hydration products such as C–S–H and AFm phases (e.g., Friedel's salt). From the standpoint of depassivation, this distinction is important because the free chloride concentration at the steel depth is more directly related to passive-film breakdown, whereas the total chloride content reflects both transport and binding within the cementitious matrix. The formal transport equations used to describe chloride ingress, binding, and their dependence on moisture state are presented in Section 4.3.

Although code provisions often adopt a single deterministic C_{crit} value, experimental evidence shows large scatter and strong dependence on the steel surface condition, electrochemical history, and the chemical state of the pore solution [4]. Consequently, there is a growing consensus that C_{crit} should be modeled as a random variable or even as a function of other state variables (e.g., pH, $[OH^-]$, or chloride-to-hydroxide ratio), rather than as a universal constant [22].

At the steel–concrete interface, chlorides promote localized breakdown of the passive film and nucleation of metastable pits. The mechanistic picture is that Cl^- ions adsorb onto the oxide film, penetrate defects, and destabilize the inner oxide by forming soluble complexes with Fe^{2+} and Fe^{3+}, which locally shifts the balance between anodic dissolution and repassivation [41]. Many pits repassivate rapidly (metastable pitting), but some reach a critical size where chemistry inside the occluded cell becomes self-sustaining (low pH, high Cl^-, limited oxygen), leading to stable pitting and progressive cross-section loss. This inherently localized nature explains why, even at chloride contents above nominal thresholds, corrosion often initiates only at specific "hot spots" along a bar rather than uniformly. From a modeling standpoint, chloride-induced depassivation therefore links continuum-scale transport and binding processes to stochastic, interface-level phenomena such as the distribution of C_{crit}, pit nucleation statistics, and local electrochemical conditions.

3.3. Combined Carbonation and Chloride Effects

In many practical exposures, carbonation and chloride ingress occur simultaneously or sequentially rather than as isolated mechanisms. Carbonation modifies both the buffering capacity and the mineralogy of the hydrated cement paste, with significant implications for chloride binding and transport [50]. Decalcification of C–S–H and decomposition of AFm phases (e.g., Friedel's and Kuzel's salts) can release previously bound chloride back into the pore solution, increasing $C_{\mathrm{Cl,free}}$ near the carbonation front.

As a result, carbonated zones may exhibit lower total chloride content but higher free-chloride concentrations and reduced pH. This combination can be particularly aggressive: reduced pH brings the system closer to the stability limit of the passive film, while increased $C_{\mathrm{Cl,free}}$ lowers the barrier for pit nucleation and growth [4, 51]. Experimental studies on specimens pre-exposed to chlorides and then carbonated (or vice versa) often show accelerated depassivation compared to purely chloridic or purely carbonated exposures, although the magnitude and direction of interaction depend on binder type, curing, and exposure history.

For modeling, combined actions raise non-trivial questions [4]: should depassivation be triggered by a pH threshold, a chloride threshold, or a combined criterion (e.g., critical $[Cl^-]/[OH^-]$ ratio)? Answering these questions consistently requires integrating thermodynamic calculations (pH, binding equilibria) with transport models and probabilistic descriptions of steel surface conditions; this integration is one of the targets for later sections of the report.

3.4. Macrocell and Microcell Corrosion; Uniform vs. Localized Attack

Even when depassivation has occurred, the spatial distribution of corrosion is governed by how anodic and cathodic reactions are arranged on the steel surface and within the structural element. Two limiting concepts are commonly distinguished [50, 52]:

- *Microcell corrosion*: small-scale anodic and cathodic sites located close to each other along the same bar, driven by very local variations in steel microstructure, passive film properties, or interfacial chemistry.
- *Macrocell corrosion*: spatially separated anodic and cathodic regions connected through electrically continuous steel and ionic conduction in the concrete pore solution, often driven by large-scale gradients in chloride concentration, moisture, oxygen availability, or temperature.

In practice, most RC structures exhibit a combination of microcells and macrocells. For instance, in a bridge deck, bars near transverse cracks or joints may act as anodic regions (high chloride, good oxygen access), while more protected regions remain predominantly cathodic; current then flows along the steel, redistributing corrosion damage away from the zones of highest chloride content. This means that local predictions of depassivation and

damage must consider not only the local chloride and pH conditions, but also the global electrical connectivity and moisture profile [41, 52].

Macrocell effects are especially important in partially repaired structures (e.g., patch repairs), where differences in concrete resistivity and chloride content between repair patches and existing material can create strong macrocell currents. From a modeling perspective, this motivates coupling transport models with spatially resolved electrochemical models (e.g., mixed-potential and Ohmic drop considerations) when aiming at realistic damage patterns rather than purely local initiation times.

The distinction between uniform and localized corrosion is closely linked to the microcell/macrocell picture. Uniform corrosion corresponds to relatively homogeneous anodic dissolution along the bar, which is rare in real structures except in some cases of carbonation-induced corrosion. Localized corrosion (pitting, crevice-like attack near air voids or cracks) is far more common for chloride-induced cases [4, 41]. From a reliability standpoint, localized loss of cross-section can be more critical than uniform thinning, because it concentrates stresses and may control ultimate capacity even when the average section loss is modest.

3.5. Nature, Volume, and Distribution of Corrosion Products

Once depassivation has occurred, iron dissolution at the anode produces Fe^{2+}, which is subsequently oxidized and precipitated as various iron oxides and oxyhydroxides, depending on pH, redox potential, chloride content, and moisture [50]. Common corrosion products in RC include:

- γ-FeOOH (lepidocrocite) and β-FeOOH (akaganeite) at relatively high chloride concentrations;
- α-FeOOH (goethite) and Fe_2O_3 (hematite) in more stable, less chloride-rich environments;
- Fe_3O_4 (magnetite) and mixed Fe(II)/Fe(III) phases at lower oxygen availability.

These phases differ in density and molar volume, leading to volumetric expansion factors on the order of 2–6 relative to the original metallic iron [41, 50].

The spatial distribution of corrosion products is equally important. Observations indicate that corrosion products do not form exclusively as a uniform ring at the steel surface; they can migrate into the steel–concrete interface (SCI) and along pores and micro-cracks, accumulating preferentially in regions of higher porosity or pre-existing voids [4]. This has several implications for modeling:

1. A portion of the corrosion products can be accommodated without generating significant mechanical stresses (“porous zone” or “diffusion zone”), delaying cracking despite ongoing corrosion.

2. Precipitation in pores can progressively clog the transport pathways, reducing oxygen and moisture access and thereby affecting the corrosion rate in a time-dependent way.
3. Heterogeneous precipitation patterns reinforce the tendency toward localized cracking and spalling, as certain segments of the bar become more confined than others.

While the detailed chemo–mechanical consequences of corrosion products (cracking, spalling, stiffness reduction) are treated in a separate report, it is important for initiation-focused models to acknowledge that the onset of significant damage is not solely a function of the amount of steel consumed, but also of where and how corrosion products are stored within the SCI and surrounding concrete [41, 50]. Capturing this interplay between chemistry, transport, and meso-structure is a key challenge for multi-physics models of corrosion-induced deterioration.

3.6. Corrosion-induced cracking and time-to-cracking models

Although the primary focus of this report is corrosion initiation, the onset of cracking in the concrete cover is the first visible manifestation of the propagation phase and is often used to define the end of service life. This subsection briefly summarizes common models for the time between depassivation and first cracking ("time-to-cracking").

Once the passive film is destroyed, the steel reinforcement begins to corrode and expansive corrosion products accumulate in the ribs and along the bar circumference. Because the molar volume of rust is several times that of the steel consumed, this accumulation generates a radial pressure on the surrounding concrete cover. When this pressure exceeds the tensile resistance of the cover, the first surface cracks appear. We denote by t_{cr} the time from depassivation to the formation of the first visible crack at the concrete surface. In the Tuutti service-life idealization discussed earlier, t_{cr} represents the dominant part of the propagation phase and strongly influences subsequent damage (cover spalling, loss of bond, and stiffness degradation).

Most models ultimately express t_{cr} in terms of a critical radial penetration (or loss of steel radius) x_0 or an equivalent critical rust production w_{cr}, together with the corrosion current density i_{corr}. Assuming a constant i_{corr}, Faraday's law gives the corrosion penetration rate. For i_{corr} expressed in $\mu\mathrm{A/cm}^2$, the penetration rate $\dot{x}$ is obtained in mm/year, so that

$$\dot{x}(t) = 0.0116\, i_{\mathrm{corr}} \quad \Rightarrow \quad t_{\mathrm{cr}} = \frac{x_0}{0.0116\, i_{\mathrm{corr}}}, \tag{17}$$

where x_0 is in mm and t_{cr} is in years.

Jamali et al. [53] grouped existing formulations into three classes: empirical, analytical, and numerical models. Below we summarize the main empirical and analytical expressions for t_{cr} (or x_0) as they are most commonly used in practice.

3.6.1. Empirical models

Empirical models are obtained by fitting experimental data from accelerated corrosion tests on beams or slabs to simple functions of cover depth c, bar diameter d, surface chloride content C_s, tensile strength f_t, and other easily measured parameters.

- **Morinaga [54].** The critical rust production per unit steel area w_{cr} is expressed as $w_{\text{cr}} = 0.0365 \times 0.602\, d\big(1+2c/d\big)^{0.85}$, which leads to

$$t_{\text{cr}} = \frac{w_{\text{cr}}}{j_r} = 0.0365\,\frac{0.602\, d\big(1+2c/d\big)^{0.85}}{j_r}, \tag{18}$$

  where j_r is the rust production rate per unit area (consistent with w_{cr}).

- **Andrade et al. [55].** Based on beam tests with impressed current,

$$t_{\text{cr}} = \frac{x_0}{0.0116\, i_{\text{corr}}}, \qquad x_0 = 0.01 \text{ mm}, \tag{19}$$

  so that t_{cr} is directly proportional to $1/i_{\text{corr}}$, and x_0 is critical attack penetration.

- **Purvis et al. [56].** From field and laboratory data the authors proposed

$$t_{\text{cr}} = \left(\frac{0.052\, c^{1.22} t_0^{0.21}}{C_s^{0.42} P_h}\right)^{0.83}, \tag{20}$$

  where t_0 is the age at the time of measuring C_s, and P_h is a water-to-cement ratio.

- **Rodriguez et al. [57] / DuraCrete [58].** The critical radial penetration x_0 is $x_0 = \big(83.8 + 7.4\,\frac{c}{d} - 22.6\, f_t\big) \times 10^{-3}$, where f_t is the splitting tensile strength. Combined with Eq. (17) this yields

$$t_{\text{cr}} = \frac{(83.8 + 7.4\, c/d - 22.6\, f_t) \times 10^{-3}}{0.0116\, i_{\text{corr}}}. \tag{21}$$

- **Alonso et al. [59].** For specimens subjected to natural corrosion, $x_0 = \big(7.53 + 9.32\,\frac{c}{d}\big) \times 10^{-3}$, and

$$t_{\text{cr}} = \frac{(7.53 + 9.32\, c/d) \times 10^{-3}}{0.0116\, i_{\text{corr}}}. \tag{22}$$

- **Webster [60].** For typical bridge decks,

$$t_{\text{cr}} = \frac{1.25\, c \times 10^{-3}}{0.0116\, i_{\text{corr}}}. \tag{23}$$

- **Torres-Acosta and Sagues [61].** Allowing for a finite corroding length L, $x_0 = 0.011\,\frac{c}{d}\left(\frac{c}{L}+1\right)^2$, and

$$t_{\text{cr}} = \frac{0.011\,(c/d)\,(c/L+1)^2}{0.0116\, i_{\text{corr}}}. \tag{24}$$

These empirical expressions highlight the dominant influence of cover-to-diameter ratio c/d, concrete tensile strength, humidity, and corrosion rate on the time-to-cracking, and they are often used in deterministic life predictions once i_{corr} has been estimated.

3.6.2. Analytical models

Analytical models start from an explicit mechanical representation of the steel–concrete system, relate a critical radial displacement or pressure to the tensile strength of the cover, and then use Faraday's law to convert the required volume of corrosion products into x_0 or t_{cr}.

- **Bažant [62].** The concrete cover is idealized as a thick-walled cylinder subjected to internal pressure from rust. The key parameter is the "hole flexibility" k, which relates radial pressure to radial displacement at the steel surface and can be written as

$$k = \frac{2d^3}{s^2 E_{\text{eff}}} + \frac{d(1+\nu_c)}{E_{\text{eff}}} + \frac{d^3}{4c(c+d)E_{\text{eff}}}, \tag{25}$$

  where s is the clear spacing between bars, E_{eff} is an effective Young's modulus, and ν_c is Poisson's ratio of the concrete.

$$t_{\text{cr}} = \left(\frac{1}{\rho_r} - \frac{\alpha_m}{\rho_s}\right)^{-1} \frac{f_t(s-d)\,k}{s\,j_r}. \tag{26}$$

  where ρ_r and ρ_s are density of rust and iron, respectively. a_m is molar mass of corrosion products to that of steel, k is hole flexibility

- **El Maaddawy and Soudki [63].** Based on thick-walled cylinder theory,

$$t_{\text{cr}} = \frac{7117.5\,(d+2\delta_0)(1+\nu_c+\psi)}{i_{\text{corr}} E_{\text{eff}}} \left[\frac{2cf_t}{d} + \frac{2\delta_0 E_{\text{eff}}}{(d+2\delta_0)(1+\nu_c+\psi)}\right] \Big/ 365, \tag{27}$$

  where E_{eff} is the effective elastic modulus of concrete, f_t is the tensile strength of concrete, d is the bar diameter, c is the concrete cover thickness, δ_0 is the corrosion penetration (loss of steel radius) at the onset of cracking, ν_c is Poisson's ratio of concrete, and ψ is a confinement parameter defined as

$$\psi = \frac{d+2\delta_0}{2c\,(c+d+2\delta_0)}. \tag{28}$$

- **Lu et al. [64].** Based on thick-walled cylinder theory,

$$t_{\text{cr}} = \frac{93905\,n\,(d+Kc)}{(24\times 365)\,(\gamma-1)\,i_{\text{corr}}} \left\{\frac{(0.3+0.6\,c/d)\,f_t}{E_{\text{eff}}} \left(\frac{b^2+a^2}{b^2-a^2}+\nu_c\right)+1\right\} \tag{29}$$

where n is moles of electrons released per mole of iron corroded, d is the bar diameter, c is the concrete cover thickness, K is an empirical coefficient that depends on the corrosion conditions, a and b are the inner and outer radii of the thick-walled cylinder, and γ is volumetric ratio of a rust product.

4. Transport of Aggressive Agents and Moisture in Concrete

This section develops physical models for the ingress of CO_2, chlorides, and moisture in cementitious materials. The ultimate goal is to predict the evolution of the environmental state (pH, chloride concentration, degree of saturation, oxygen availability) at the steel–concrete interface, which controls the onset of depassivation and subsequent corrosion. Emphasis is placed on chloride-bearing exposures, with carbonation and coupled mechanisms treated consistently but with less detail.

4.1. Pore Structure, Moisture States, and Degree of Saturation

As discussed in Section 2.1.3, the hydrated cement paste contains a connected pore network spanning gel pores, capillary pores, and larger voids. The porosity ϕ_p and degree of saturation S were defined previously in Eq. (3). Together, they determine the amount of liquid water available for transport and the extent to which the pore network is active for diffusion and flow. For corrosion initiation, these quantities are particularly important because they influence chloride ingress, oxygen availability, and internal relative humidity at the steel–concrete interface.

Experimentally, pore-size distribution, connectivity, and moisture-dependent occupancy can be characterized using techniques such as mercury intrusion porosimetry, nitrogen sorption, backscattered electron image analysis, and X-ray tomography [25, 50, 65]. For transport, it is convenient to distinguish between:

- *total porosity* (all pores, including isolated ones), and
- *transport porosity* (pores belonging to a percolating network that can carry liquid water, ions, or gas).

Percolation-based models show that, even at fixed total porosity, connectivity and tortuosity of the transport network can vary significantly with water-to-cement ratio, degree of hydration, and curing, leading to order-of-magnitude differences in effective diffusivity [50, 65].

Tortuosity τ is often introduced as a geometric factor that increases the effective path length for diffusing species compared with a straight-line distance. At the continuum scale, τ is usually accounted for implicitly through an effective diffusion coefficient D_{eff}, but conceptually it is useful to think of D_{eff} as

$$D_{\text{eff}} \sim \frac{\phi_{\text{conn}}}{\tau} D_{\text{pore}}, \tag{30}$$

where ϕ_{conn} is the connected porosity and D_{pore} is a molecular diffusivity in the pore fluid. Micro-structural changes due to hydration, supplementary cementitious materials, carbonation, or leaching effectively act by modifying ϕ_{conn} and τ over time [50, 66].

For moisture, a central quantity is the degree of saturation S, as defined in Eq. (4). By definition $0 \leq S \leq 1$, with $S = 1$ corresponding to fully water-saturated pores, and $S \approx 0$ to an almost dry material. In practice, concrete in service rarely reaches either extreme; instead, it cycles through intermediate saturation states as a function of exposure climate, member geometry, and transport histories.

The pore water in concrete can be present in different moisture states, which strongly influence both transport and electrochemical processes [50, 66]:

- *Chemically bound water*: incorporated in hydrates; does not participate directly in transport on service-life time scales.
- *Adsorbed water*: physisorbed on solid surfaces in gel pores and small capillaries at low to intermediate relative humidity; contributes to mass and mechanical properties but has limited mobility.
- *Capillary water*: liquid water in capillary pores and larger voids; main carrier for ionic transport (chlorides, alkalies, calcium, etc.).
- *Water vapour*: gaseous phase in partially saturated pores; controls drying, internal humidity, and condensation processes.

Thermodynamically, the equilibrium between pore liquid and vapour at a given temperature T and relative humidity RH can be related to the capillary (suction) pressure p_c via the Kelvin equation:

$$p_c = -\frac{RT}{V_w} \ln(\text{RH}), \tag{31}$$

where R is the gas constant and V_w is the molar volume of water. Eq. (31) shows that lower RH corresponds to higher suction, which tends to empty larger capillaries first, leaving only tightly held adsorbed water in small pores at very low RH. Conversely, at high RH approaching saturation, capillary condensation fills increasingly finer pores, increasing S and enabling liquid-phase connectivity across the microstructure.

The relationship between θ (or S) and RH at fixed temperature is described by a sorption isotherm $\theta(\text{RH})$ (or $S(\text{RH})$). In cementitious materials, this relation is nonlinear, exhibits hysteresis between drying and wetting paths, and depends on pore structure and binder composition [66]. In the context of corrosion, sorption isotherms are essential because they link environmental relative humidity and temperature to the internal moisture state, which in turn controls:

- the connectivity of liquid water pathways that conduct chlorides and other ions;
- the effective diffusivity and permeability for CO_2 and O_2;

- the electrical resistivity of concrete, influencing macrocell formation and corrosion kinetics.

For chloride-induced depassivation, intermediate to high degrees of saturation are typically the most damaging: sufficient liquid water must be present to transport dissolved chlorides to the steel surface, but complete saturation can limit oxygen supply and slow corrosion kinetics [4, 41, 50]. A realistic service life model must therefore treat $S(x,t)$ (or $\theta(x,t)$) as an evolving state variable coupled to the external climate, not as a fixed parameter.

4.2. Governing Concepts for Moisture Transport

Moisture transport in concrete is intrinsically multiphase: liquid water and water vapour coexist and move through a deformable porous skeleton, with phase exchange (evaporation/condensation) and temperature effects. Rigorous descriptions are available within the framework of unsaturated porous media mechanics, but for service-life modeling it is common to employ reduced formulations that retain the key dependencies while remaining computationally tractable [41, 50].

At the continuum scale, conservation of water mass in a representative elementary volume can be written schematically as

$$\frac{\partial \theta}{\partial t} \;=\; -\nabla\cdot\mathbf{J}_\ell - \nabla\cdot\mathbf{J}_v + q, \tag{32}$$

where $\mathbf{J}_\ell$ and $\mathbf{J}_v$ are the fluxes of liquid water and water vapour (per unit area and time), respectively, and q accounts for sinks/sources (e.g. binding or release of water in hydration, which is often neglected beyond early ages). In many long-term durability applications, temperature gradients are modest and the vapour term can be lumped into an effective moisture flux, leading to simplified "moisture diffusion" formulations of the form

$$\frac{\partial \theta}{\partial t} \;=\; \nabla\cdot\left(D_\theta(\theta)\,\nabla\theta\right), \quad \text{or} \quad \frac{\partial \mathrm{RH}}{\partial t} \;=\; \nabla\cdot\left(D_{\mathrm{RH}}(\mathrm{RH})\,\nabla\mathrm{RH}\right), \tag{33}$$

where $D_\theta(\theta)$ or $D_{\mathrm{RH}}(\mathrm{RH})$ are effective moisture diffusion coefficients that embed the influence of pore structure, tortuosity, and the interplay between liquid and vapour transport.

More advanced models distinguish explicitly between liquid flow and vapour diffusion. Liquid transport is typically described by a Richards-type relationship,

$$\mathbf{J}_\ell \;=\; -K(h)\left(\nabla h + \mathbf{e}_g\right), \tag{34}$$

where $K(h)$ is the unsaturated hydraulic conductivity, h is the hydraulic head, and $\mathbf{e}_g$ represents gravity effects. Through the moisture-retention relation, K may equivalently be expressed as a function of water content or degree of saturation.

Vapour flux is described by Fickian diffusion in the gas-filled porosity,

$$\mathbf{J}_v \;=\; -D_v(S)\,\nabla c_v, \tag{35}$$

where D_v is a vapour diffusivity (strongly decreasing with increasing S) and c_v is vapour concentration. Through the Kelvin Eq. (31), these formulations can be recast in terms of $\mathrm{RH}(x,t)$ as the primary variable, leading back to an effective diffusivity description as in Eq. (33) but with parameters that can, in principle, be related to measurable transport and sorption properties.

For corrosion modeling, the level of detail chosen for moisture transport must be consistent with the intended use:

- In simplified service-life approaches, S is often treated as a constant, and climatic effects enter only through time-invariant "exposure class" parameters for chloride diffusion and carbonation.
- In more mechanistic models, $\mathrm{RH}(x,t)$ or $S(x,t)$ is explicitly computed via Eq. (33) (or a Richards-type formulation) with boundary conditions driven by ambient climate (temperature, relative humidity, rainfall), and the resulting moisture field is used to update chloride diffusivity $D_{\mathrm{eff}}(S)$, oxygen and CO_2 transport, and concrete resistivity [41, 50].

In the present report, moisture transport is primarily discussed at the level of Eq. (33), with $D_{\mathrm{RH}}(\mathrm{RH})$ calibrated from sorption and drying tests, as this provides a useful reduced description for engineering applications. The resulting $\mathrm{RH}(x,t)$ field may then be used to modulate (i) effective chloride diffusion coefficients, (ii) carbonation rates, and (iii) oxygen availability at the steel depth.

4.3. Chloride Transport: Diffusion, Migration, Convection, and Binding

At structural scale, chloride ingress in concrete is most often modeled as a one–dimensional transport problem through the cover under exposure to a chloride-bearing environment (marine spray, tidal or splash zones, de-icing salts, etc.). The simplest idealization considers a semi-infinite slab with an initially chloride-free profile, subject to a constant surface concentration C_s and governed by Fick's second law with a constant apparent diffusion coefficient D_{app}:

$$\frac{\partial C}{\partial t} = \frac{\partial}{\partial x}\left(D_{\mathrm{app}}\frac{\partial C}{\partial x}\right), \qquad C(x,0)=0, \qquad C(0,t)=C_s, \tag{36}$$

where $C(x,t)$ denotes the total chloride content at depth x and exposure time t [50, 67]. Under these assumptions, Eq. (36) admits the classical error-function solution

$$C(x,t) = C_s\left[1-\mathrm{erf}\left(\frac{x}{2\sqrt{D_{\mathrm{app}}t}}\right)\right], \tag{37}$$

which underlies many code-type approaches and inverse analyses of chloride profiles [68]. In this setting, D_{app} is an effective transport parameter fitted from experiments; it implicitly accounts for porosity, tortuosity, chloride binding, and, to some extent, concrete aging.

Aging effects (continued hydration, pozzolanic reactions) are often represented by a time-dependent apparent diffusion coefficient,

$$D_{\mathrm{app}}(t) \;=\; D_{\mathrm{ref}} \left(\frac{t}{t_{\mathrm{ref}}} \right)^{-m}, \tag{38}$$

where D_{ref} is the apparent diffusion coefficient at a reference age t_{ref} (e.g. 28 or 90 days) and m is an aging exponent typically in the range 0.1–0.5, depending on binder type and curing [50, 68]. In practice, Eqs. (36)–(38) form the backbone of many service-life models: they provide a convenient closed-form description for $C(x,t)$ and allow direct estimation of corrosion initiation time by comparing C at the bar depth with a critical chloride threshold, C_{crit}.

A more mechanistic treatment distinguishes between free and bound chlorides. The total chloride content can be written as

$$C_{\mathrm{tot}} \;=\; C_{\mathrm{free}} + C_b(C_{\mathrm{free}}), \tag{39}$$

where C_{free} denotes the concentration of chloride ions in the pore solution and C_b is the bound fraction associated with C–S–H and AFm phases [24, 66]. In many models, C_b is represented by an empirical binding isotherm (linear, Freundlich, Langmuir), calibrated from paste or mortar tests. Conservation of chloride mass can then be expressed as

$$\frac{\partial C_{\mathrm{tot}}}{\partial t} \;=\; \frac{\partial}{\partial x} \left(D_{\mathrm{eff}}(S,T) \frac{\partial C_{\mathrm{free}}}{\partial x} \right), \tag{40}$$

where D_{eff} is an effective diffusivity that depends on degree of saturation S and temperature T. Using Eq. (39), Eq. (40) can be rewritten in terms of C_{free}:

$$\left(1 + \frac{\partial C_b}{\partial C_{\mathrm{free}}} \right) \frac{\partial C_{\mathrm{free}}}{\partial t} \;=\; \frac{\partial}{\partial x} \left(D_{\mathrm{eff}}(S,T) \frac{\partial C_{\mathrm{free}}}{\partial x} \right). \tag{41}$$

The factor

$$\beta_b(C_{\mathrm{free}}) = \frac{\partial C_b}{\partial C_{\mathrm{free}}}$$

acts as a "buffer" coefficient: strong binding (large β_b) slows changes in C_{free} for a given change in C_{tot} and can thus be interpreted as reducing the effective rate of increase of free chloride at the steel depth [24, 66]. In terms of an apparent diffusion concept, Eq. (41) shows that binding lowers an effective diffusion coefficient by a factor $(1+\beta_b)^{-1}$, which justifies the use of experimentally calibrated D_{app} that implicitly accounts for binding.

For more advanced applications, chloride transport is treated within a multi-ionic Nernst–Planck framework. In that case, each ionic species i (e.g. Cl^-, Na^+, K^+, OH^-, Ca^{2+}) has a flux

$$\mathbf{J}_i \;=\; -D_i \nabla c_i - z_i u_i F c_i \nabla \phi_e + c_i \mathbf{v}, \tag{42}$$

where D_i is a diffusion coefficient, c_i the concentration, z_i the charge number, u_i a mobility, F Faraday's constant, ϕ_e the electrical potential, and $\mathbf{v}$ a Darcy-scale convective velocity of the pore solution [39]. Eq. (42) for all species are combined with electroneutrality and appropriate chemical equilibrium relations (including binding), and solved numerically at the continuum scale [39].

Convection and capillary suction can also contribute to chloride transport, particularly under wetting–drying cycles. When liquid water moves with velocity $\mathbf{v}_\ell$ (e.g. due to capillary suction during wetting), the free-chloride balance acquires an advective term:

$$\frac{\partial C_{\text{free}}}{\partial t} \;=\; -\nabla\cdot\left(-D_{\text{eff}}(S,T)\nabla C_{\text{free}} + C_{\text{free}}\mathbf{v}_\ell\right) + (\text{binding terms}). \tag{43}$$

Such convection–diffusion formulations have been used to capture enhanced chloride penetration along preferential paths and during repeated wetting events in splash and tidal zones [69]. When concrete is nearly saturated and hydraulic gradients are small, $\mathbf{v}_\ell$ is often negligible and Eq. (40) suffices; in partially saturated or strongly cycled conditions, however, the convective term can be important.

Boundary conditions at the exposed surface are another key modeling choice. In many design-oriented approaches, a Dirichlet condition is adopted,

$$C_{\text{tot}}(x=0,t) = C_s, \tag{44}$$

with C_s taken as constant or piecewise constant in time. More refined models employ a flux (Robin) condition to represent finite surface mass-transfer resistance and time-varying surface chloride content,

$$-D_{\text{eff}}\frac{\partial C_{\text{free}}}{\partial x}\Big|_{x=0} = \alpha\big(C_{\text{env}}(t) - C_{\text{free}}(0,t)\big), \tag{45}$$

where α is a surface exchange coefficient and $C_{\text{env}}(t)$ reflects the external chloride level (e.g. seasonal de-icing cycles or tidal immersion histories) [68]. The choice of boundary condition has a direct impact on predicted surface gradients and thus on time-to-initiation estimates.

In summary, chloride transport models span a spectrum from simple Fickian formulations with constant D_{app} and Dirichlet boundary conditions to fully coupled, multi-ionic, convection–diffusion–reaction models. The present report adopts a layered approach: we start from the Fickian baseline for transparency and analytical insight, then progressively introduce binding, aging, moisture coupling, and (where justified) convective effects, with a view toward probabilistic service-life assessment for chloride-induced depassivation.

4.4. Carbonation Modeling and CO_2 Transport

Compared with chloride ingress, modeling of carbonation has traditionally relied more on empirical laws, especially the widely used $\sqrt{t}$-relationship, as discussed in Eq. (16)

[50, 51]. This equation can be rationalized by considering CO_2 diffusion into a semi-infinite domain with a reaction front that moves inward as portlandite and other hydrates are consumed. In design practice, k_{carb} is often calibrated from accelerated or natural carbonation tests and adjusted for environmental factors (e.g. sheltering from rain, relative humidity, CO_2 concentration).

More mechanistic models treat carbonation as a coupled transport–reaction process. At the simplest level, CO_2 is assumed to diffuse through the gas-filled porosity and, to a lesser extent, in the aqueous phase, with a sink term representing reactions with portlandite and C–S–H:

$$\frac{\partial C_{\mathrm{CO_2}}}{\partial t} = \nabla\cdot\left(D_{\mathrm{CO_2}}(S)\,\nabla C_{\mathrm{CO_2}}\right) - R_{\mathrm{carb}}(C_{\mathrm{CO_2}}, C_{\mathrm{Ca(OH)_2}}, C_{\mathrm{C\text{–}S\text{–}H}}), \tag{46}$$

where $C_{\mathrm{CO_2}}$ is the concentration of CO_2 in the pore space, $D_{\mathrm{CO_2}}(S)$ is an effective diffusion coefficient strongly dependent on degree of saturation S, and R_{carb} is a reaction rate term that consumes CO_2 and hydrates [70, 71]. The dependence on S reflects the fact that CO_2 transport is hindered at very high saturation (gas pathways blocked) and at very low saturation (limited dissolution and reaction), with an optimum in the intermediate humidity range.

In more elaborate formulations, Eqs. (32) and (46) are solved simultaneously, along with an energy balance, to capture interactions between CO_2 diffusion, moisture transport, heat transfer, and evolving microstructure [71–73]. The chemical subsystem includes at least the dissolution of CO_2 in pore solution (Henry's law), acid–base equilibria of carbonate species, and dissolution/precipitation of portlandite and decalcification of C–S–H. In such coupled models, carbonation is not represented by a sharp front; instead, a finite reaction zone forms where pH, porosity, and phase assemblage evolve gradually.

A conceptually distinct but related class of models uses a moving-boundary formulation: carbonation is represented as an interface separating carbonated and uncarbonated zones, and the interface motion is governed by a Stefan-type condition balancing diffusive flux of CO_2 with the stoichiometric demand of the reaction [70, 73]. In the limit of constant material properties, this approach recovers the $\sqrt{t}$-law, but it also provides a framework for incorporating time-varying transport properties and reaction capacities.

From a corrosion-initiation perspective, the main outputs of interest from carbonation models are: (i) the time evolution of the carbonation depth $x_{\mathrm{carb}}(t)$ relative to cover thickness and bar location; and (ii) the associated evolution of pH and chloride-binding capacity in the affected zone [50, 51]. In this report, we emphasise chloride-induced depassivation and therefore treat carbonation at a level that is sufficient to quantify when the steel–concrete interface enters a lower-pH regime; the detailed consequences of carbonation for mechanical performance and transport (e.g. porosity changes, shrinkage) are left to complementary documents.

4.5. Coupled Moisture, Heat, and Multi-Ion Transport

The separate treatments of moisture, chloride, and CO_2 transport in the preceding subsections are convenient idealizations. In real structures subjected to wetting–drying, temperature cycles, and mixed ionic environments, these processes are strongly coupled. Degree of saturation $S(x,t)$, temperature $T(x,t)$, and the concentrations of multiple ionic species $\{c_i(x,t)\}$ (e.g., Cl^-, OH^-, Na^+, K^+, Ca^{2+}, HCO_3^-, SO_4^{2-}) evolve simultaneously and interact through their influence on transport coefficients, reaction rates, and electrochemical equilibria [39, 50].

At the continuum scale, a generic coupled formulation can be written in terms of a vector of primary variables

$$\mathbf{u}(x,t) = \big[\theta(x,t),\, T(x,t),\, c_1(x,t), \ldots, c_N(x,t)\big]^{\mathsf{T}},$$

where θ is the volumetric water content, T the temperature, and c_i the concentrations of N ionic species. Conservation of water mass is expressed by Eq. (32), with fluxes $\mathbf{J}_\ell$ and $\mathbf{J}_v$ derived from the unsaturated flow laws introduced earlier. Conservation of each ionic species i is usually based on the Nernst–Planck flux, Eq. (42), combined with electroneutrality and chemical-equilibrium relations for binding and complexation [39]. An energy balance completes the system, for example in the form

$$\rho c_p \frac{\partial T}{\partial t} \;=\; \nabla\cdot\big(k_T \nabla T\big) + L_v \frac{\partial \theta}{\partial t} + q_T, \tag{47}$$

where ρ is density, c_p specific heat, k_T an effective thermal conductivity, L_v the latent heat of evaporation/condensation, and q_T accounts for external heat sources or sinks [50].

The principal couplings may be summarized as follows:

- Moisture content θ (and S) influences effective diffusivities $D_{\text{eff}}(S,T)$ for ionic species, as well as $D_{CO_2}(S)$ in Eq. (46), by opening or closing liquid and gas pathways.
- Temperature T affects diffusivities, hydraulic conductivity, and ionic mobilities, and enters reaction kinetics (e.g., carbonation, hydration, chloride binding) via Arrhenius-type factors.
- Ionic composition controls osmotic suction and, through electroneutrality and acid–base equilibria, the pH and buffering capacity of the pore solution.
- The electrical potential field $\phi_e(x,t)$, determined implicitly by charge conservation and boundary conditions, feeds back into the ionic fluxes in Eq. (42).

Numerical implementations range from tightly coupled, monolithic finite-element formulations to staggered solution schemes in which moisture, temperature, and ion transport are iterated within each time step [39]. For realistic exposure scenarios (e.g., tidal zones, bridge decks with seasonal de-icing), such coupled models are often the only way to represent the

combined effects of non-isothermal wetting–drying cycles, variable surface salinity, and changing degree of saturation. However, they also require significantly more input data and calibration than the simpler Fickian models discussed earlier. In this report we limit explicit multi-ion–thermal couplings to selected illustrative cases and otherwise embed their effects in effective transport parameters that depend on S and T.

4.6. Influence of Mix Design, SCMs, and Concrete Type

The transport parameters appearing in Eqs. (33), (41), and (46) are not intrinsic constants; they depend strongly on mix design, binder composition, aggregate properties, and curing. From a depassivation standpoint, the most important material influences are: (i) the evolution of pore structure and connectivity; (ii) the chloride- and carbonate-binding capacity; and (iii) the alkalinity and buffering capability of the pore solution [15, 50].

The water-to-binder ratio (w/b) governs the initial capillary porosity and, together with the degree of hydration, controls the percolation threshold and tortuosity of the transport network [15]. Lower w/b generally leads to reduced connected porosity, smaller effective diffusivities D_{eff}, and lower moisture permeability, but may also increase autogenous shrinkage and cracking if not properly cured. Aggregate type and grading influence both the microstructure of the interfacial transition zone and the overall tortuosity of the pore system; dense, non-reactive aggregates combined with good packing tend to reduce transport, whereas porous or reactive aggregates can introduce additional pathways and chemical interactions [15, 50].

Supplementary cementitious materials such as fly ash, slag, silica fume, and metakaolin generally refine the pore structure at medium to long ages, reduce $D_{\text{app}}(t)$ in Eq. (38), and can significantly enhance resistance to chloride ingress [50, 74]. Slag and certain fly ashes increase the alumina content of the hydrate assemblage and thereby the capacity to form AFm phases (e.g., Friedel's salt), enhancing chloride binding; silica fume, by contrast, contributes little alumina but strongly densifies the ITZ and bulk paste. These benefits are often offset by slower early-age hydration and, in some cases, a reduction in portlandite content, which can increase carbonation susceptibility if cover is insufficient or curing is poor [50, 74]. One consequence is that the aging exponent m in Eq. (38) is not universal: SCM-rich concretes may exhibit relatively high D_{app} at early ages but a steeper decay over time.

Concrete type (normal-strength vs. high-performance, lightweight vs. normal-weight, self-compacting vs. vibrated) also affects transport. High-performance concretes with low w/b and silica fume typically show very low chloride diffusivities and moisture permeabilities, but may have more pronounced self-desiccation and shrinkage tendencies [15]. Lightweight aggregates can act as internal curing reservoirs, modifying moisture distributions and thereby influencing both transport and electrochemical conditions at the reinforcement [50]. Curing conditions (duration and effectiveness of moist curing, temperature history) strongly influence the degree of hydration, micro-cracking, and ITZ quality, and

thus must be reflected in initial values and early evolution of transport parameters.

For long-term modeling, these mix-design effects are commonly incorporated through:

- time-dependent diffusion and permeability functions (e.g., Eq. (38) with mix-dependent D_{ref} and m);
- binder-specific chloride-binding isotherms $C_b(C_{\text{free}})$;
- distinct carbonation coefficients k_{carb} in Eq. (16), reflecting different portlandite contents and pore structures.

In the context of probabilistic service life assessment, it is therefore essential to treat mix-design parameters not merely as deterministic inputs but as sources of epistemic uncertainty (in specified properties) and aleatory variability (in as-built quality) that propagate into predicted depassivation times.

4.7. Environmental Exposure Scenarios and Boundary Conditions

The final ingredient in transport modeling is the representation of environmental exposure as boundary conditions for the governing equations. Design standards such as EN 206, fib Model Code 2010, and similar documents classify exposures into broad classes (e.g., atmospheric carbonation, marine splash, tidal, submerged, de-icing, indoor) based on the dominant deterioration mechanisms and characteristic moisture and chloride loads [50, 75]. Translating these qualitative classes into quantitative boundary conditions for Eqs. (33), (41), and (46) is a non-trivial but crucial step.

For carbonation, the boundary conditions are typically formulated in terms of ambient CO_2 concentration (or partial pressure), relative humidity, and temperature histories at the exposed surface. For chloride ingress, boundary conditions specify the surface chloride content and its temporal evolution, plus the near-surface moisture state. For a one-dimensional cover model, a generic set of boundary conditions at $x = 0$ may include:

- a prescribed or flux-type moisture boundary, coupling interior $\text{RH}(0,t)$ to ambient $\text{RH}_\infty(t)$ and rainfall;
- a Dirichlet or Robin condition for chloride (cf. the previous subsection), with a time-varying surface concentration $C_s(t)$ representing, for example, intermittent de-icing or seasonal variation in seawater salinity;
- a surface CO_2 concentration $C_{\text{CO}_2,\infty}(t)$ linked to outdoor or indoor air composition and ventilation;
- a thermal boundary reflecting air temperature, solar radiation, and long-wave exchange, which controls $T(0,t)$.

Different exposure scenarios correspond to different combinations and statistics of these boundary functions. Atmospheric urban exposures might be characterized by moderate

CO_2 levels, moderate RH, and rare wetting; marine splash zones by frequent wetting–drying cycles with high $C_s(t)$; tidal zones by periodic immersion and drying, with rapidly varying $S(0,t)$; and indoor exposures by relatively stable temperature and RH but possibly elevated CO_2 for poorly ventilated spaces [50]. In service-life calculations, it is common to idealize these histories as stationary stochastic processes or as representative periodic cycles (daily or seasonal).

5. Deterministic Models for Corrosion Initiation

In this section, the qualitative mechanisms and transport models presented earlier are translated into quantitative frameworks for predicting the time to depassivation (corrosion initiation). We begin with deterministic formulations based on threshold concepts, which can later be relaxed and extended within probabilistic and spatially explicit models.

5.1. Threshold-Based Concepts for Depassivation

Most deterministic service life models for reinforced concrete adopt a *threshold-based* view of corrosion initiation: corrosion is assumed to remain negligible as long as a protective state variable (e.g., pH) is above a critical level, or as long as an aggressive variable (e.g., chloride concentration) remains below a critical value at the steel depth. Depassivation is then defined as the first time at which one of these scalar thresholds is violated. Formally, if $\mathbf{y}(x,t)$ denotes the local environmental state at the steel–concrete interface (e.g., pH, C_{free}, degree of saturation, potential), and $g(\mathbf{y})$ is a scalar indicator of passivity, then the deterministic initiation time t_{init} can be written as

$$t_{\text{init}} \;=\; \inf\left\{t \geq 0 : g\big(\mathbf{y}(x_{\text{steel}},t)\big) \leq g_{\text{crit}}\right\}, \tag{48}$$

where inf means infimum (the greatest lower bound of a set of numbers), x_{steel} is the nominal bar depth and g_{crit} is a prescribed threshold value. In practical models this generic expression is instantiated in simpler forms, most commonly through chloride- or carbonation-based criteria.

5.1.1. Critical chloride content

For chloride-induced corrosion, the prevailing threshold concept is the *critical chloride content* C_{crit} [4, 22]. Two main variants are used in the literature and in codes:

- a threshold expressed as total chloride relative to cement mass, $C_{\text{crit}}^{\text{mass}}$ (e.g., % Cl^- by mass of cement), and
- a threshold expressed as free chloride concentration in the pore solution, $C_{\text{crit}}^{\text{free}}$ (e.g., mol/L).

In terms of the chloride transport models, a deterministic chloride-based initiation time is commonly defined as

$$t_{\text{init}}^{\text{Cl}} \;=\; \inf\left\{ t \geq 0 : C_{\text{free}}(x_{\text{steel}}, t) \;=\; C_{\text{crit}}^{\text{free}} \right\}, \tag{49}$$

or, in a mass-based form,

$$t_{\text{init}}^{\text{Cl}} \;=\; \inf\left\{ t \geq 0 : \frac{C_{\text{tot}}}{m_{\text{cement}}}(x_{\text{steel}}, t) \;=\; C_{\text{crit}}^{\text{mass}} \right\}, \tag{50}$$

where C_{free} and C_{tot} are the free and total chloride contents at the steel depth (cf. Eq. (39)), and m_{cement} is the cement mass associated with the sampling volume [50]. These expressions link the deterministic initiation time directly to the chosen transport model and surface boundary conditions.

A more mechanistic alternative uses a chloride-to-hydroxide ratio threshold, recognizing that the stability of the passive film depends on both chloride and alkalinity. In that case, the condition in Eq. (48) is specialized to

$$\frac{[\text{Cl}^-]}{[\text{OH}^-]}(x_{\text{steel}}, t) \;=\; \left(\frac{[\text{Cl}^-]}{[\text{OH}^-]} \right)_{\text{crit}}, \tag{51}$$

with the understanding that both numerator and denominator evolve with time and depth [22]. In practice, however, the experimental determination of separate $[\text{Cl}^-]$ and $[\text{OH}^-]$ at the bar depth is challenging, and many deterministic models revert to simpler $C_{\text{crit}}^{\text{mass}}$ or $C_{\text{crit}}^{\text{free}}$ formulations calibrated from laboratory or field data.

A central difficulty, emphasized by Angst et al. [22], is that measured C_{crit} values exhibit large scatter (often spanning at least an order of magnitude) and depend on a host of factors not captured in a single scalar quantity: steel composition and surface condition, prior electrochemical history, concrete mix and pore solution chemistry, moisture state, and measurement procedure. Angst [4] therefore argue that the notion of a unique, universal C_{crit} is untenable; instead, one should view C_{crit} as a steel- and system-specific parameter, and ultimately as a random variable. In the deterministic framework of this section, however, a single representative value (or a small set of values for different exposure classes and steel types) is typically adopted.

In support of this probabilistic viewpoint, Figure 7 illustrates cumulative distributions of corrosion initiation vs. measured chloride content from several widely cited experimental datasets and model assumptions. Laboratory data by Breit and Zimmermann show markedly different median values and spreads despite broadly similar exposure conditions, while the fib Model Code curve and Vassie's field observations indicate even larger scatter at the structural scale. Together, these distributions are influenced by specimen geometry, steel surface condition, and test protocol.

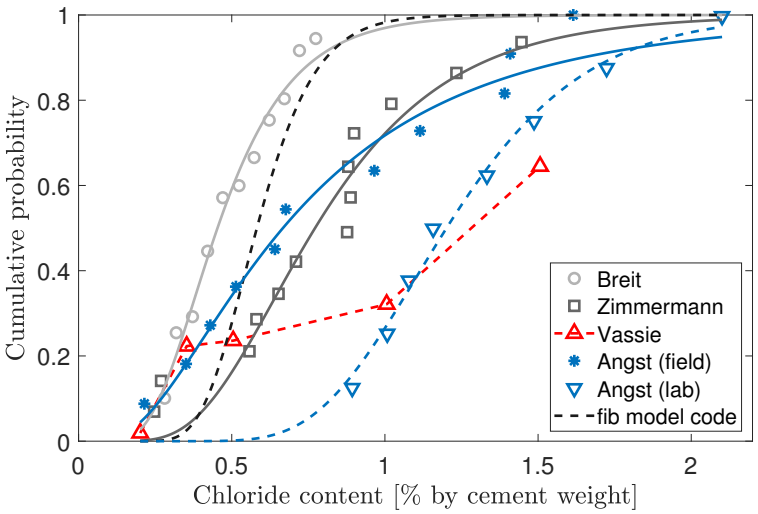

Fig. 7. Cumulative probability of corrosion initiation versus chloride content from selected laboratory and field datasets, together with a code-based distribution; adapted from [8, 9].

5.1.2. Carbonation depth and critical pH

For carbonation-induced depassivation, threshold-based models usually rely on the position of the carbonation front relative to the bar depth [50, 51]. If $x_{\mathrm{carb}}(t)$ denotes the carbonation depth (e.g., based on phenolphthalein indicator) and c the nominal cover, the simplest deterministic initiation time is

$$t_{\mathrm{init}}^{\mathrm{carb}} \;=\; \inf\{t \geq 0 : x_{\mathrm{carb}}(t) \;=\; c\}\,, \tag{52}$$

with $x_{\mathrm{carb}}(t)$ often represented by the $\sqrt{t}$-law in Eq. (16). This implicitly assumes that (i) the pH drops from its initial value (≈ 13) to some lower level (often taken as 9–10) at the carbonation front, and (ii) depassivation occurs once that front reaches the steel.

More refined criteria incorporate the local pH explicitly, for instance by defining a critical pH pH_{crit} below which the passive film cannot be sustained:

$$pH(x_{\mathrm{steel}}, t_{\mathrm{init}}^{\mathrm{carb}}) \;=\; pH_{\mathrm{crit}}. \tag{53}$$

This opens the possibility of accounting for gradual pH gradients and diffuse carbonation fronts, rather than a sharp interface [51]. In practice, however, field identification of pH_{crit} is even more difficult than for chloride thresholds, and most deterministic models revert to Eq. (52) as a proxy.

5.1.3. Limitations of scalar thresholds

While threshold-based concepts provide a simple and intuitive link between transport models and initiation time, they also introduce important limitations. First, the threshold is usually defined in terms of a local quantity at a single depth and point along the bar, whereas

real structures exhibit significant spatial variability in chloride content, pH, moisture state, and steel surface condition. Corrosion will in general initiate at the most unfavourable location, which may correspond to a small region where conditions locally exceed the nominal threshold well before the mean profile does. This creates a gap between deterministic, one-dimensional profiles and three-dimensional, spatially heterogeneous initiation patterns.

Second, a single scalar threshold cannot capture the combined effects of multiple interacting variables. For example, the critical chloride content clearly depends on pH and the chemical state of the pore solution, meaning that different combinations of C_{Cl} and pH may lead to depassivation or continued passivity [4, 51]. Similarly, moisture and temperature influence both transport and electrochemical kinetics, yet are rarely incorporated explicitly in threshold definitions.

Third, the threshold concept is intrinsically linked to the experimental protocol used to identify it; the same physical system may yield different apparent C_{crit} values depending on whether corrosion onset is detected by half-cell potential, corrosion current, visual inspection, or mass loss, and depending on whether total or free chlorides are measured [22, 50]. These methodological dependencies must be borne in mind when selecting threshold values for deterministic models.

Despite these limitations, threshold-based formulations remain the backbone of most deterministic service life models and design recommendations. They offer a transparent way to connect transport calculations to initiation times and to compare the relative performance of different mix designs and cover thicknesses.

5.2. Time-to-Initiation Models under Chloride Exposure

When chloride ingress is the dominant mechanism, deterministic time-to-initiation models couple a transport description for $C_{\mathrm{Cl}}(x,t)$ with a threshold criterion such as Eqs. (49) or (50). The simplest and still most widely used class of models is based on the error-function solution Eq. (37) of Fick's law Eq. (36), supplemented by empirical adjustments for aging and binding [3, 50, 75].

5.2.1. Closed-form Fickian solutions

For a semi-infinite cover, initially free of chlorides, exposed to a constant surface concentration C_s and described by a constant apparent diffusion coefficient D_{app}, the solution Eq. (37) gives the total chloride content at the steel depth x_{steel} as

$$C(x_{\mathrm{steel}},t) = C_s\left[1-\operatorname{erf}\left(\frac{x_{\mathrm{steel}}}{2\sqrt{D_{\mathrm{app}}t}}\right)\right]. \tag{54}$$

Equating this to a mass-based critical value $C_{\text{crit}}^{\text{mass}}$ and solving for t yields a closed-form expression for the deterministic initiation time:

$$t_{\text{init}}^{\text{Cl}} = \frac{x_{\text{steel}}^2}{4D_{\text{app}}} \left[\text{erf}^{-1}\left(1 - \frac{C_{\text{crit}}^{\text{mass}}}{C_s}\right) \right]^{-2}, \tag{55}$$

provided $0 < C_{\text{crit}}^{\text{mass}} < C_s$ [67].

As a simple numerical illustration of Eq. (55), we consider a semi-infinite concrete cover with bar depth $x_{\text{steel}} = 50$ mm, subject to a constant surface chloride content C_s and an apparent diffusion coefficient $D_{\text{app}} = 5 \times 10^{-12}\,\text{m}^2/\text{s}$. Chloride is normalized by C_s and the critical value is set to $C_{\text{crit}} = 0.6C_s$, which yields a deterministic initiation time $t_{\text{init}}^{\text{Cl}}$ of 28.8 years. The corresponding closed-form solution is evaluated over depths $x \in [0, 80]$ mm and times $t \in [0, 50]$ years to generate the profiles and contour shown in Figure 8.

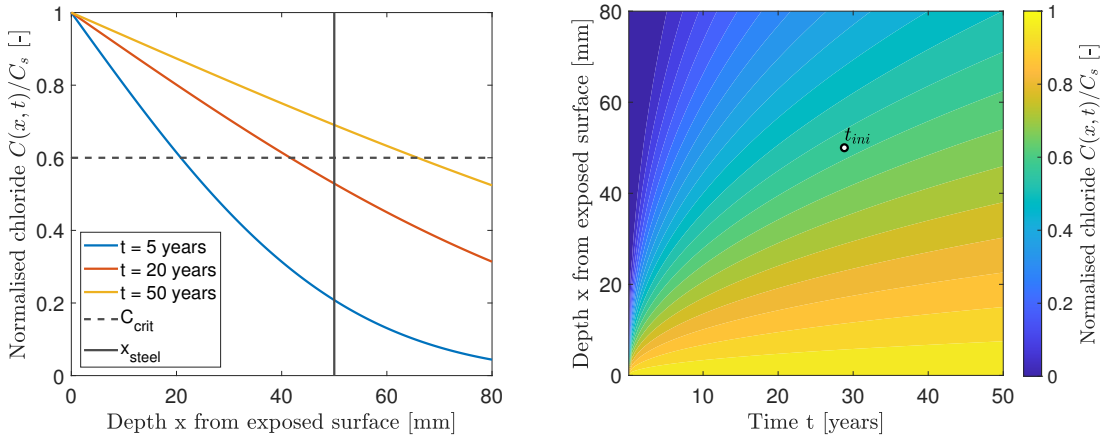

(a) Normalised profiles $C(x,t)/C_s$ versus depth at $t = 5$, 20, and 50 years

(b) Contour plot of $C(x,t)/C_s$ in the (t,x)-plane

Fig. 8. Closed-form Fickian chloride ingress for a semi-infinite cover.

Variants of Eq. (55), sometimes with empirical correction factors, underpin many design-oriented service life models, including those in national codes and in durability design tools such as DuraCrete and Life-365 [50, 75].

In cases where the surface concentration C_s is not constant, but tends towards a limiting value $C_{s,\infty}$, it is common to replace C_s in Eq. (55) by an effective time-dependent or averaged surface value, or to introduce a time-varying boundary condition of Robin type and solve numerically for $C(x_{\text{steel}}, t)$. Analytical solutions for such cases are restricted to special forms of $C_s(t)$ and are rarely used directly in design [67].

5.2.2. Incorporating aging, binding, and moisture dependence

In practice, the apparent diffusion coefficient is strongly age- and binder-dependent (Eq. (38)), and binding modifies the evolution of free chloride according to Eq. (41). A common en-

gineering approach is to retain the error-function structure but replace D_{app} in Eq. (55) by an equivalent value that captures aging and binding over the relevant period. For instance, if $D_{\text{app}}(t)$ follows Eq. (38), one may define a time-averaged diffusion coefficient

$$\bar{D}(t) = \frac{1}{t}\int_0^t D_{\text{app}}(\tau)\,\mathrm{d}\tau, \tag{56}$$

and use $\bar{D}(t_{\text{init}}^{\text{Cl}})$ as a surrogate for D_{app} in Eq. (55), together with an empirically calibrated exponent m for the specific mix and curing conditions [50, 75]. Binding may be reflected either by adjusting C_{crit} (e.g., working with free vs. total chlorides) or by embedding the buffering factor $(1+\beta_b)^{-1}$ into an effective diffusion parameter, based on isotherm data for the binder system considered [24, 66].

A further refinement is to let D_{eff} depend on degree of saturation and temperature, $D_{\text{eff}}(S,T)$, with $S(x,t)$ and $T(x,t)$ computed from moisture and heat transport models such as Eq. (33) and (47). In that case, Eq. (41) is solved numerically in space and time, and $t_{\text{init}}^{\text{Cl}}$ is obtained as the first time at which $C_{\text{free}}(x_{\text{steel}},t)$ reaches $C_{\text{crit}}^{\text{free}}$. Such coupled models are necessary for exposures with strong wetting–drying or temperature cycles, where $D_{\text{eff}}(S,T)$ can vary by orders of magnitude over a year [39, 68].

5.2.3. Convection and non-Fickian effects

In zones with significant liquid movement (wicking, capillary suction, drainage), advective transport contributes to chloride ingress, leading to convection–diffusion equations of the type Eq. (43). Here the time-to-initiation problem has no useful closed-form solution; instead, numerical methods (finite elements or finite volumes) are employed to compute $C_{\text{free}}(x,t)$ under realistic boundary conditions, including time-varying surface salinity and moisture [69, 76]. Non-Fickian features such as anomalous diffusion, preferential transport paths, and multi-scale heterogeneities are sometimes represented through fractional-order models or multi-layer systems, but these remain largely research-oriented.

5.2.4. Existing service life models

The conceptual structure described above appears, with varying levels of refinement, in a number of established service-life models and design recommendations. Tuutti's original framework [3] separated the initiation and propagation phases and implicitly assumed Fickian transport to define $t_{\text{init}}^{\text{Cl}}$. The fib Model Code [75] and related documents formalize this into partial-factor design expressions, linking cover, D_{app}, C_s, and C_{crit} to initiation time, sometimes in probabilistic form. Dedicated tools such as Life-365 and DuraCrete implement more elaborate parameter sets (binder-specific aging functions, climatological data, etc.) but remain rooted in the same deterministic core: a Fickian or Fickian-like transport model combined with a scalar chloride threshold at the steel depth.

5.3. Time-to-Initiation Models under Carbonation

For carbonation-dominated environments, deterministic models for depassivation time are similarly built by combining a description of the carbonation front (or pH evolution) with a threshold condition such as Eq. (52). The simplest models rely on the empirical $\sqrt{t}$-law Eq. (16); more mechanistic approaches derive $x_{\mathrm{carb}}(t)$ or $pH(x,t)$ from the CO_2 transport and reaction equations.

5.3.1. Empirical $\sqrt{t}$-based models

If $x_{\mathrm{carb}}(t)$ is represented by $x_{\mathrm{carb}}(t) = k_{\mathrm{carb}}\sqrt{t}$, then Eq. (52) gives immediately

$$t_{\mathrm{init}}^{\mathrm{carb}} = \left(\frac{c}{k_{\mathrm{carb}}}\right)^2, \tag{57}$$

where c is the nominal concrete cover [50].

Different exposure conditions (outdoor vs. indoor, sheltered vs. unsheltered, varying CO_2 concentration and humidity) are reflected in different values of k_{carb}, often obtained from accelerated or natural carbonation tests and adjusted by empirical correction factors [70, 71].

Eq. (57) is widely used in standards and guidelines because of its transparency and direct link between cover thickness and initiation time. However, it hides a number of assumptions: constant material properties, constant environmental conditions, a relatively sharp carbonation front, and a fixed pH drop at that front. Furthermore, the influence of moisture is only indirectly captured via the calibrated k_{carb}, even though relative humidity strongly affects both CO_2 transport and reaction rates [51].

5.3.2. PDE-based carbonation models

More mechanistic approaches derive $x_{\mathrm{carb}}(t)$ from transport–reaction equations such as Eq. (46), coupled with moisture transport and, in some cases, heat transfer [71, 72]. In such models, carbonates form gradually over a finite reaction zone, and pH decreases continuously rather than discontinuously at a sharp front. A practical definition of carbonation depth must therefore be chosen, for example as the location where pH drops below a chosen threshold (e.g. 10) or where a certain fraction of portlandite is consumed. Once this operational $x_{\mathrm{carb}}(t)$ is defined, Eq. (52) or an equivalent pH-based condition can be used to compute $t_{\mathrm{init}}^{\mathrm{carb}}$.

In moving-boundary formulations, the carbonation front is treated explicitly as an interface whose motion is governed by a balance between diffusive CO_2 flux and the stoichiometric demand of the hydrates [70, 73]. In the limit of constant material properties, this again leads to a $\sqrt{t}$-law, but with k_{carb} expressed in terms of CO_2 diffusivity, effective reaction rate, and reactant capacity. This provides a more rational basis for assessing the influence

of mix design and environmental conditions on carbonation kinetics than purely empirical fits.

5.3.3. Moisture and exposure dependence

Because CO_2 transport occurs primarily in the gas-filled porosity, while carbonation reactions occur in the aqueous phase, degree of saturation plays a central role in carbonation models. At very high S, gas pathways are blocked and CO_2 ingress is slow; at very low S, dissolution and reaction are limited; an intermediate range of RH typically maximizes carbonation rate [51]. PDE-based models incorporate this through $D_{CO_2}(S)$ and possibly through R_{carb} in Eq. (46), whereas empirical models subsume it into k_{carb} via exposure class–specific calibration.

For long-term predictions, both empirical and mechanistic models must also account for changes in environmental conditions over time (e.g., urbanisation, indoor climate control, climate change) and for material aging (e.g., ongoing hydration, micro-structural refinement, changes in chloride-binding capacity) [50]. In a deterministic setting, these influences are typically represented by piecewise constant or slowly varying parameters (e.g., different k_{carb} values for different phases of exposure). In more advanced frameworks, environmental histories are fed into coupled transport–reaction models, and t_{init}^{carb} is computed directly from the evolving pH or carbonation depth at the steel depth.

In all cases, the core structure mirrors that of chloride-induced initiation: a transport or front-propagation model for the relevant aggressive agent (CO_2 here), a local depassivation criterion (formulated in terms of depth or pH), and a definition of initiation time as the earliest time at which the criterion is violated at the reinforcement location.

5.4. Multivariate and Mechanistic Criteria

The threshold-based formulations in Eqs. (49)–(52) implicitly assume that a single scalar quantity (e.g., chloride content or carbonation depth) suffices to characterize the depassivation condition. Experimental and field evidence, however, indicate that corrosion initiation depends on the joint state of several variables, including chloride concentration, pH, steel potential, moisture, oxygen availability, and steel surface condition [4, 22, 50]. This has motivated a range of multivariate and more mechanistic criteria, sometimes summarized under the heading “beyond the chloride threshold”.

A conceptual generalization of Eq. (48) is to define initiation through an explicit multiparameter limit state. Let

$$\mathbf{y}(t) = \big(C_{Cl}(x_{steel},t),\, pH(x_{steel},t),\, E_{corr}(t),\, S(x_{steel},t)\big) \tag{58}$$

collect the chloride content (free or total), pH, corrosion potential, and degree of saturation at the steel depth. A multivariate initiation criterion can then be written in terms of a limit

state function $G(\mathbf{y})$,

$$G\big(\mathbf{y}(t_{\text{init}})\big) = 0, \qquad G(\mathbf{y}) > 0 \text{ for passivity}, \quad G(\mathbf{y}) < 0 \text{ for active corrosion.} \tag{59}$$

In principle, G could be derived from mechanistic electrochemical models (e.g., mixed potential theory, local pit stability analyses), but in practice it is often constructed empirically by correlating measured onset of corrosion with combinations of C_{Cl}, pH, E_{corr}, and moisture in laboratory or field exposures [4, 22].

One simple example is a depassivation criterion expressed in the chloride–pH plane. Rather than prescribing a fixed $C_{\text{crit}}^{\text{free}}$, a family of critical combinations $\big(C_{\text{Cl}}^{\text{crit}}, pH^{\text{crit}}\big)$ is defined, for instance in the form of an iso-line $C_{\text{Cl}}^{\text{crit}} = f(pH)$ inspired by Pourbaix-type considerations and experimental data [4, 50]. In that setting, chloride-induced depassivation at the steel depth is taken to occur when the state trajectory $\big(C_{\text{Cl}}(t), pH(t)\big)$ crosses the critical curve in the plane, rather than when C_{Cl} alone exceeds a constant threshold. This is conceptually consistent with the known dependence of passive-film stability on both chloride activity and alkalinity.

More mechanistic criteria focus on localized pit stability. Classical pitting models distinguish between conditions for pit initiation (nucleation of metastable pits) and conditions for pit propagation (transition to stable pits of increasing depth). Within this view, steel remains effectively passive if any nascent pits repassivate rapidly; depassivation in the structural sense corresponds to the formation of at least one stable pit above some critical size. Mechanistic pit-stability criteria can be expressed in terms of a critical repassivation potential E_{rep} or pitting potential E_{pit}, or in terms of local balances between dissolution and mass-transport rates within a pit cavity [50]. In reinforced concrete, such detailed electrochemical modeling is complicated by the spatially heterogeneous environment at the steel–concrete interface, but the underlying idea is clear: initiation is controlled not solely by bulk C_{Cl} or pH, but by local conditions at the pit mouth and inside the pit.

From a modeling standpoint, multivariate and mechanistic criteria such as Eq. (59) are attractive because they can, in principle, account for:

- the combined effects of chloride, pH, moisture, and oxygen on passive-film stability;
- the influence of steel potential and polarization behavior on pit nucleation and growth;
- the distinction between transient metastable pitting and sustained, structurally relevant depassivation.

Their main drawbacks are the increased data requirements (to identify G) and the difficulty of calibrating such models for realistic field conditions.

5.5. Uniform vs. Localized Initiation and Representative Volume Elements

The deterministic formulations above implicitly assume that corrosion initiation occurs "uniformly" along the reinforcing bar at the depth considered. In reality, depassivation

is almost always localized: small regions with unfavourable micro-environments (higher chloride, lower pH, lower resistivity, surface defects) become anodic, while adjacent regions remain passive and act as cathodes [4, 50]. This raises a modeling question: how should such localized initiation be represented within continuum-scale service-life models?

A useful conceptual device is the representative volume element (RVE) at the steel–concrete interface. One may imagine discretizing the steel surface into surface patches of area A_{RVE} (or length L_{RVE} for a 1D representation), each of which is large enough to contain many micro-cells (local anodic and cathodic sites) but small enough to capture spatial variability in exposure and material properties. At the scale of an RVE, one can then define a local initiation condition of the form

$$G_{\mathrm{loc}}\big(\mathbf{y}_{\mathrm{loc}}(t)\big) = 0, \tag{60}$$

analogous to Eq. (59) but with RVE-averaged state variables $\mathbf{y}_{\mathrm{loc}}$. The global initiation time for a member or structural detail is then associated with the RVE that first reaches its local depassivation condition.

In a purely deterministic setting, this localization can be represented phenomenologically by introducing a localization factor that relates the local condition at the worst-affected RVE to the averaged condition predicted by a one-dimensional cover model. For instance, one might write

$$C_{\mathrm{Cl,loc}}(x_{\mathrm{steel}},t) = \gamma_{\mathrm{loc}}\, C_{\mathrm{Cl,1D}}(x_{\mathrm{steel}},t), \tag{61}$$

with $\gamma_{\mathrm{loc}} > 1$ representing the amplification of chloride content in a locally unfavourable patch compared with the 1D-averaged profile [50]. An analogous factor could be applied to pH or to other state variables. In practice, γ_{loc} is difficult to calibrate and is often replaced by implicit conservatism in the choice of C_{crit} or cover depth.

A more systematic approach, which will be developed in later sections, treats local initiation times as random variables defined over the steel surface. At the scale of an RVE, one can associate a local initiation time $T_{\mathrm{init}}^{(k)}$ to each patch k and view the structural initiation time as the minimum over all patches,

$$t_{\mathrm{init,\,struct}} = \min_{k} t_{\mathrm{init}}^{(k)}. \tag{62}$$

Even if each $t_{\mathrm{init}}^{(k)}$ is governed by a simple local threshold (e.g., a local C_{crit}), the distribution of the minimum depends on the number of patches and on the spatial correlation structure, leading naturally to an extreme-value description of localized initiation. From the continuum modeling viewpoint, the notion of an RVE then serves as a bridge between detailed spatial variability and the global initiation time relevant for engineering decisions.

For deterministic service life analysis, it is sufficient to recognize explicitly that (i) initiation is governed by localized conditions at small regions of the bar; (ii) one-dimensional cover models predict spatial averages that must be interpreted with care; and (iii) any scalar

C_{crit} or pH_{crit} used in design inevitably embeds assumptions about localization and RVE size. Clarifying these assumptions is an important step toward developing multi-scale, probabilistic models in which localized depassivation at the steel surface can be represented more faithfully.

6. Multiphysics PDE Frameworks and Numerical Implementation

This section collects the transport and initiation concepts introduced above into a modular system of governing equations and discusses how that system may be implemented numerically. The overall philosophy follows the framework discussed in [77] for chloride ingress, carbonation, and corrosion in reinforced concrete, which itself builds on classic contributions by [67, 71, 78–80]. The intent is not to prescribe a single numerical scheme, but rather to define a coupled PDE framework that can be discretized using different methods depending on the geometry, exposure scenario, and desired level of fidelity.

6.1. Governing Equations for Coupled Transport and Corrosion

A common starting point in hygro–thermal and transport modeling of concrete is the generic conservation law used, for example, by [78, 79]:

$$\frac{\partial b_k}{\partial t} + \nabla \cdot \mathbf{J}_k = r_k, \qquad k = 1, \ldots, n_{\text{eq}}, \tag{63}$$

where b_k is a storage term (e.g., water content, total chloride per unit volume, heat content), $\mathbf{J}_k$ the corresponding flux, and r_k a source/sink term due to reactions.

In the present context, we are interested in the following primary fields:

- pore relative humidity $RH(\mathbf{x},t)$ or water content $W(\mathbf{x},t)$;
- temperature $T(\mathbf{x},t)$;
- free and total chloride concentrations $C_{\text{free}}(\mathbf{x},t)$ and $C_{\text{tot}}(\mathbf{x},t)$;
- dissolved CO_2 concentration $g(\mathbf{x},t)$ and degree of carbonation $c(\mathbf{x},t)$;
- (optionally) concentrations of other ions, $c_{\alpha(\mathbf{x},t)}$;
- corrosion current density $i_{\text{corr}}(\mathbf{x},t)$ and metal loss $z_{\text{steel}}(\mathbf{x},t)$ on the steel surface.

6.1.1. Moisture and heat

The coupled moisture–heat equations [71, 79] can be written in the generic form Eq. (63) with:

- a moisture balance for the water content $W(RH,T)$, with flux given by a Darcy–type law plus vapour diffusion, and

- a heat balance for the enthalpy $h(RH,T)$, with Fourier heat conduction and latent heat terms.

Because these equations and constitutive relations are taken directly from [71, 79], we refer to them as the moisture and heat subsystem $[RH,T]$ in the present report.

6.1.2. Chloride transport with binding

For chloride transport, we rely on the Xi–Bažant model [78, 80] and its implementation in [77]. For unsaturated concrete, the chloride transport equation can be written as

$$\frac{\partial C_{\text{free}}}{\partial t} = \frac{\partial C_{\text{free}}}{\partial C_{\text{tot}}} \left[\nabla \cdot \left(D_{\text{Cl}} \nabla C_{\text{free}} \right) + \mu \, \frac{\partial W}{\partial t} \, C_{\text{free}} \right], \tag{64}$$

where C_{free} is the free chloride concentration in the pore solution, C_{tot} is the total chloride content per unit volume of concrete, μ is a coefficient coupling advective transport to changes in water content (as in [78, 80]), and $W(RH,T)$ is the water content governed by the moisture equation.

The apparent chloride diffusivity D_{Cl} is typically expressed as a multiplicative function of humidity, temperature and concrete age, following Xi–Bažant and related work:

$$D_{\text{Cl}}(RH,T,t_e) = D_{\text{Cl,ref}} \, f_{RH}(RH) \, f_T(T) \, f_{\text{age}}(t_e), \tag{65}$$

where $D_{\text{Cl,ref}}$ is a reference diffusivity (e.g., at a given reference humidity, temperature and age), and f_{RH}, f_T and f_{age} are empirical correction functions calibrated from laboratory or field data [77, 78, 80]. The exact functional forms may vary between authors, but the multiplicative structure Eq. (65) is standard. Here, $f_{\text{age}}(t_e)$ should be understood as an empirical, matrix-dependent correction that reflects aging effects such as continued hydration and microstructural refinement. In practice, the multiplicative form in Eq. (65) is a convenient engineering approximation; however, it assumes that the influences of humidity, temperature, and age can be separated, whereas interactions between aging and moisture state may require recalibration or a more mechanistic treatment for specific binder systems.

From Eq. (39), total chloride is decomposed into free and bound parts, with C_b described by a Freundlich isotherm,

$$C_b(C_{\text{free}}) = K_{\text{Fr}} C_{\text{free}}^{n_{\text{Fr}}}, \tag{66}$$

where K_{Fr} and n_{Fr} are material parameters identified from binding tests. The corresponding factor obtained from the binding relation and entering Eq. (64) is then

$$\frac{\partial C_{\text{free}}}{\partial C_{\text{tot}}} = \left(1 + \frac{\mathrm{d}C_b}{\mathrm{d}C_{\text{free}}} \right)^{-1} = \left(1 + n_{\text{Fr}} K_{\text{Fr}} C_{\text{free}}^{n_{\text{Fr}}-1} \right)^{-1}. \tag{67}$$

In the multi-physics framework, Eq. (64) represents one of the k-equations in the generic balance form Eq. (63), coupled to the moisture equation through $W(RH,T)$ and to temperature through the factor $f_T(T)$ in $D_{\text{Cl}}(RH,T,t_e)$.

6.1.3. CO_2 transport and carbonation

For carbonation, we adopt the diffusion–reaction model of [71, 79], also used in [77]. The governing diffusion–reaction equation for dissolved CO_2 is

$$\frac{\partial g}{\partial t} = \nabla\cdot\big(D_g \nabla g\big) - \frac{\partial g_c}{\partial t}, \tag{68}$$

with consumption term

$$\frac{\partial g_c}{\partial t} = \alpha_4 \frac{\partial c}{\partial t}, \tag{69}$$

and carbonation rate

$$\frac{\partial c}{\partial t} = \alpha_1 f_1(RH)\, f_2(g)\, f_3(c)\, f_4(T), \tag{70}$$

where α_1 is a kinetic rate coefficient for carbonation and α_4 is a stoichiometric conversion coefficient relating the rate of carbonation to the rate of dissolved CO_2 consumption; the humidity, CO_2, carbonation-degree, and temperature functions f_1–f_4 are given in Eqs. (71)–(74).

$$f_1(RH) = \begin{cases} 0, & 0 \le RH \le 0.50, \\ 2.5\,(RH - 0.50), & 0.50 < RH < 0.90, \\ 1, & 0.90 \le RH \le 1.00, \end{cases} \tag{71}$$

$$f_2(g) = \frac{g}{g_{\max}}, \tag{72}$$

$$f_3(c) = 1 - R^m, \qquad R = \frac{c}{c_{\max}}, \tag{73}$$

$$f_4(T) = A \exp\left(-\frac{E_0}{RT}\right), \tag{74}$$

The CO_2 diffusivity $D_g(RH, T, t_e, c)$ follows the multiplicative Eq. law (75).

$$D_g(RH, T, t_e, c) = D_{g,28}\, F_1^*(RH)\, F_2(T)\, F_3(t_e)\, F_4(c), \tag{75}$$

$$F_1^*(H) = (1 - H)^{2.5}, \tag{76}$$

$$F_2(T) = \exp\left(\frac{Q}{RT_0} - \frac{Q}{RT}\right), \tag{77}$$

$$F_3(t_e) = \chi + (1 - \chi)\sqrt{\frac{28}{t_e}}, \tag{78}$$

$$F_4(c) = 1 - \zeta R, \qquad R = \frac{c}{c_{\max}}, \tag{79}$$

where $D_{g,28}$ is the diffusivity of carbon dioxide in the standard condition (28 days curing, temperature = 25^oC).

6.1.4. Multi-ion transport

When a more detailed treatment of the pore solution is needed, chloride can be embedded into a multi-ion Nernst–Planck model [81]. The flux of ionic species α may be written as

$$\mathbf{J}_\alpha = -D_\alpha \nabla c_\alpha - z_\alpha u_\alpha F\, c_\alpha \nabla \phi_e + c_\alpha \mathbf{v}_w, \tag{80}$$

where α indexes the ionic species, D_α is the diffusion coefficient, c_α the concentration, z_α the charge number, u_α the ionic mobility, F the Faraday constant, ϕ_e the electric potential, and $\mathbf{v}_w$ the Darcy-scale pore-solution velocity. Combined with the conservation Eq.law (63) and appropriate electroneutrality constraints, Eq. (80) provides a more mechanistic multi-ion description consistent with the chloride-only model when other ions are lumped into effective diffusivities [81].

6.1.5. Corrosion current and metal loss (Faraday's law)

At the steel surface, the link between corrosion current and metal loss follows directly from Faraday's law [82, 83]. The local rate of steel cross-section loss x_{steel} is

$$\dot{x}_{\text{steel}} = \frac{M_{\text{Fe}}}{nF\rho_{\text{Fe}}}\, i_{\text{corr}}, \tag{81}$$

where M_{Fe} is the molar mass of iron, n the number of electrons ($n = 2$ for $\text{Fe}\rightarrow\text{Fe}^{2+}$), F Faraday's constant, and ρ_{Fe} the density of steel. In the framework discussed in [77], i_{corr} is evaluated using electrochemical models and empirical relationships linked to chloride, pH and moisture at the steel depth, and then Eq. (81) is used to drive rust expansion and steel area loss in subsequent mechanical analyses.

6.2. Boundary and Initial Conditions for Realistic Exposures

The mass- and energy-balance equations above must be complemented by initial and boundary conditions that reflect the intended exposure scenario. Here we follow the classifications used in [67, 77–79].

6.2.1. Initial conditions

A typical choice is a spatially uniform state representing the condition at the start of aggressive exposure, for example

$$\begin{aligned} H(\mathbf{x},0) &= H_0, \\ T(\mathbf{x},0) &= T_0, \\ C_{\text{free}}(\mathbf{x},0) &= C_{\text{free},0}, \\ g(\mathbf{x},0) &= g_0. \end{aligned} \tag{82}$$

with $H_0, T_0, C_{\text{free},0}, g_0$ taken from curing conditions or pre-exposure laboratory measurements. For structures with strong pre-existing gradients (e.g., partially carbonated covers),

piecewise linear profiles for $c(x,0)$ and $g(x,0)$, as used by Saetta et al. [79], can also be adopted here.

6.2.2. Dirichlet boundary conditions

Classic diffusion problems and many laboratory tests use prescribed surface concentrations, the classical form in [67]. For chloride ponding, [78, 80] impose

$$C_{\text{free}}(\mathbf{x},t) = C_s \qquad \text{on } \Gamma_D^{\text{Cl}}, \tag{83}$$

with C_s constant or piecewise constant in time. Similarly, Saetta et al. [79] use fixed external CO_2 concentration and relative humidity on exposed faces for carbonation simulations.

6.2.3. Neumann and Robin (flux/convective) boundary conditions

When surface fluxes are measured or when convective exchange with the environment is more realistic, Neumann or Robin boundary conditions are used. For chloride, a pure Neumann condition reads

$$-\mathbf{n}\cdot D_{\text{Cl}}\nabla C_{\text{free}} = q_{\text{Cl}}(t) \qquad \text{on } \Gamma_N^{\text{Cl}}, \tag{84}$$

where $\mathbf{n}$ denotes the outward unit normal vector to the boundary, and q_{Cl} the imposed inward flux. For CO_2, a Robin condition of the following form is adopted

$$-\mathbf{n}\cdot D_g\nabla g = h_g\left(g_{\text{env}}(t) - g\right), \tag{85}$$

where h_g is a mass-transfer coefficient and $g_{\text{env}}(t)$ is the external CO_2 concentration history. Analogous convective forms are standard for heat and moisture exchange, with (h_T, T_{env}) and (h_H, H_{env}), respectively [77, 79].

6.2.4. Exposure scenarios

Different service environments correspond to different combinations of the above boundary conditions:

- *Stationary laboratory tests*: constant C_s, H_{env}, T_{env} and g_{env}, typically with a step at $t = 0$.
- *Cyclic wetting–drying*: periodic variation of $C_s(t)$ and $H_{\text{env}}(t)$ in Eq. (83) and its moisture analogue, as in [78].
- *Marine splash and tidal zones*: combinations of Dirichlet and Robin conditions on different faces, with time-varying wetting and drying periods [80].
- *Partially sheltered structures*: reduced h and/or lower C_s on sheltered faces, following the practice in [77].

6.3. Spatial and Temporal Discretization

Once the governing equations and boundary conditions are specified, numerical solution proceeds by spatial and temporal discretization. At this stage, the framework remains methodologically flexible: finite element, finite volume, or finite difference approximations may all be appropriate, depending on the structure of the governing equations, the complexity of the geometry, the required conservation properties, and the intended engineering application.

6.3.1. Semi-discrete form

In their finite element formulations of hygro–thermal and carbonation problems, [71, 79] obtain semi-discrete systems of the form

$$\mathbf{M}\,\dot{\mathbf{u}} + \mathbf{K}(\mathbf{u})\,\mathbf{u} = \mathbf{f}(\mathbf{u}, t), \tag{86}$$

where $\mathbf{u}$ collects nodal values of the primary unknowns (e.g. H, T, g, C_f), $\mathbf{M}$ is a capacity matrix (depending on storage terms such as $W(H,T)$ or C_t), $\mathbf{K}(\mathbf{u})$ is a stiffness-like matrix assembled from the flux terms (diffusivities, permeabilities, conductivities), and $\mathbf{f}(\mathbf{u},t)$ gathers boundary and source contributions. This form Eq. (86) is standard in finite element treatments of coupled transport and is also used in [77].

6.3.2. Finite differences and finite volumes

For 1D and simple 2D geometries, finite difference or finite volume schemes are commonly used for chloride transport, as in [78, 80], leading to discrete analogues of Eq. (64) with central differences for diffusion and explicit or implicit time-stepping. The same discretization ideas apply to the CO_2 Eq. (68). Finite volume formulations are particularly natural when Eq. (63) is written explicitly in conservative form.

6.3.3. Time integration

For the stiff couplings present in chloride, moisture and CO_2 transport, the references cited above typically use implicit time integration: backward Euler or Crank–Nicolson schemes in [67], and fully implicit schemes in [78, 79]. In [77], a backward Euler step is combined with Newton or Picard iterations to update D_{Cl}, D_g and the binding capacity at each time step.

7. Experimental and Monitoring Data for Model Calibration

While this report is primarily modeling-oriented, realistic prediction of corrosion initiation requires parameters, boundary data, and validation targets anchored in experiments and field observations. This section reviews the most relevant laboratory and in-situ techniques and explains how their outputs map onto the parameters of the transport and initiation models introduced in the preceding sections. The focus is not on test procedures

themselves (which are governed by standards and recommendations), but on their role in informing effective diffusivities, sorptivities, binding parameters, surface concentrations, environmental histories, and corrosion indicators.

7.1. Laboratory Characterization of Transport Properties

Laboratory tests on concretes and mortars provide the primary data for estimating effective transport coefficients and related quantities. From the perspective of the models in this report, three families of tests are particularly important: diffusion and migration tests for ionic transport, absorption/sorptivity tests for capillary ingress, and permeability-type tests for gas and liquid flow.

7.1.1. Diffusion and migration tests.

Classical immersion or bulk-diffusion tests expose one face of a specimen to a chloride solution for a given duration, then measure the chloride profile with depth. Standards such as ASTM C1556 [84] describe procedures for extracting powder samples at discrete depths and determining the acid-soluble chloride content. The apparent diffusion coefficient D_{app} is then obtained by fitting the error-function solution of Fick's second law [67] to the measured profile (with or without correction for binding), making these tests directly compatible with the Fickian-based time-to-initiation models discussed earlier.

Non-steady-state migration tests provide a faster alternative by applying an electric field across a saturated specimen and measuring the penetration depth of chlorides after a fixed time. The widely used NT BUILD 492 method yields a non-steady-state migration coefficient D_{nssm} from a closed-form expression based on the measured penetration depth, temperature and test duration. Rapid chloride permeability tests such as ASTM C1202 [85] measure the total charge passed (in coulombs) under a fixed voltage; although this is not a diffusion coefficient in a strict sense, empirical correlations and calibration curves are often used to infer an equivalent conductivity or to classify concretes into qualitative "low-moderate-high" permeability ranges.

7.1.2. Sorptivity and capillary suction

Water absorption and sorptivity tests quantify the rate at which water is drawn into unsaturated concrete by capillary suction. ASTM C1585 [86], for example, measures the cumulative mass of water absorbed per unit area as a function of the square root of time, and defines the initial sorptivity S from the slope of the linear portion of this curve. In the context of transport modeling, sorptivity is directly related to the capillary conductivity and to the effective permeability function in the moisture equation, and thus constrains the parameters governing the evolution of H and W in partially saturated covers.

7.1.3. Permeability and gas transport

Gas-permeability tests, often using oxygen or air flow under a pressure gradient, provide information on the connectivity of the pore network at low saturation. While such tests are not tied to a single standard, their outputs can be mapped to intrinsic permeability values that enter Darcy-type formulations for gas or vapour flow. Combined with sorptivity data, they help calibrate the humidity-dependent transport functions used in chloride and carbonation models.

7.1.4. Chloride binding tests

Binding isotherms are obtained by equilibrating powdered cementitious material with chloride solutions of different concentrations, then measuring the free and bound fractions. Fitting Freundlich or Langmuir isotherms to these data provides the parameters (e.g., A and B in the Freundlich law) that appear in the binding-capacity expression $\partial C_f/\partial C_t$ and therefore control the effective diffusivity and storage terms in the chloride transport equation. When possible, binding tests should be performed on materials with similar binder composition, curing and exposure as the structural concrete of interest.

7.2. Field Exposure Sites and Chloride/Carbonation Profiles

Laboratory tests provide controlled, short-term measurements, but the long-term evolution of chloride ingress and carbonation is best captured by field exposure sites and in-situ sampling of existing structures. From the modeling viewpoint, such data deliver both effective transport parameters and realistic boundary and initial conditions.

7.2.1. Chloride profiles in field-exposed elements

In marine or de-icing environments, cores or powder samples are extracted at various depths from exposed faces of beams, columns, bridge decks, or dedicated exposure blocks. The total chloride content is commonly determined according to standards such as ASTM C1152 [87], and plotted as a function of cover depth and exposure time. These profiles can be fitted with Fickian (or extended) solutions to back-calculate effective diffusion coefficients and surface concentrations under field conditions, which often differ substantially from laboratory values due to variable humidity, temperature, cracking, and micro-structural evolution.

7.2.2. Carbonation depths and pH indicators

For carbonation, the standard practice is to split cores or slices and spray the freshly exposed surface with a pH indicator such as phenolphthalein. The boundary between colored and uncolored regions provides an estimate of the carbonation depth, which can be monitored over time for different exposure classes (indoor, outdoor sheltered, outdoor unsheltered, etc.). These measurements can be compared against the $\sqrt{t}$ empirical laws or against

the CO_2 diffusion–reaction models introduced earlier, with the observed scatter reflecting both material variability and environmental fluctuations.

7.2.3. Thermogravimetric and microstructural analyses

Thermogravimetric analysis (TGA), X-ray diffraction (XRD) and related methods on drilled powder samples permit quantification of portlandite content, calcium carbonate, and other phases, thereby providing indirect measures of degree of carbonation or leaching. In chloride-exposed concretes, TGA can be used to quantify chloride-bearing solid phases such as Friedel's salt, but it does not directly distinguish free chloride from total bound chloride. When combined with complementary chemical or pore-solution measurements, however, it can support an indirect assessment of chloride binding. Such data are valuable for validating reaction terms and phase-evolution assumptions in coupled transport–chemistry models, albeit at the expense of significant laboratory effort.

7.3. Electrochemical and Electrical Monitoring Techniques

Electrochemical and electrical methods probe the corrosion state and the transport properties of concrete non-destructively or with minimal intrusion. They play a dual role in model calibration: (i) as indicators of whether depassivation has occurred and (ii) as indirect measures of parameters such as concrete resistivity or corrosion current density.

7.3.1. Half-cell potential mapping

Half-cell potential measurements, standardized for example in ASTM C876 [88], map the corrosion potential of reinforcing bars relative to a reference electrode on the concrete surface. Spatial patterns of potential can identify regions with high likelihood of active corrosion, especially when combined with information on moisture and chloride exposure. While absolute potentials are affected by many factors, they provide qualitative validation targets for initiation models and help identify areas where more detailed measurements are needed.

7.3.2. Concrete resistivity

Electrical resistivity of concrete, measured with surface four-point (Wenner) probes or embedded sensors, is a key parameter for both corrosion and transport modeling. Low resistivity is associated with higher ionic mobility and corrosion rates, whereas high resistivity suggests limited transport and slow corrosion. Empirical correlations are widely used in practice to classify corrosion risk based on resistivity ranges, and these values can also be used to bound effective diffusion coefficients in numerical models.

7.3.3. Polarization resistance and Stern–Geary relation

Linear polarization resistance (LPR) tests apply a small potential perturbation around the corrosion potential and measure the resulting current. The slope of the potential–current curve near the corrosion potential defines the polarization resistance R_p, which can be related to the corrosion current density i_{corr} via the Stern–Geary equation [89]:

$$i_{\text{corr}} = \frac{B}{R_p}, \tag{87}$$

where B is a constant that depends on the Tafel slopes of the anodic and cathodic reactions. In reinforced concrete applications, typical values of B are taken from experimental studies (e.g., [83]), and the resulting i_{corr} estimates provide direct input for Faraday's law and corrosion rate models.

7.3.4. Impedance spectroscopy and advanced methods

Electrochemical impedance spectroscopy (EIS) measures the frequency-dependent response of the steel–concrete system to a small alternating current (AC) perturbation and can separate contributions from charge transfer, diffusion (Warburg impedance) and concrete resistivity [90]. Although EIS is more complex to interpret and less common in routine practice, it offers rich information that can be used to calibrate mechanistic models of the steel–concrete interface and to validate assumptions about the coupling between transport and electrochemistry. Electrical resistivity tomography and embedded sensor networks extend these ideas to spatial mapping of resistivity and moisture, supporting model validation at member scale.

7.4. Accelerated Corrosion and Transport Tests

Because natural corrosion and transport processes in concrete are slow, accelerated tests are often used to generate data within feasible laboratory time frames. From a modeling standpoint, such tests are useful for parameter identification, but care is required when extrapolating to natural exposures.

7.4.1. Impressed-current corrosion tests

In impressed-current tests, a constant or controlled current is applied between the reinforcing bar (anode) and an auxiliary electrode (cathode), forcing corrosion at a rate much higher than in natural conditions. The resulting crack patterns, rust volumes and loss of cross-section can be measured and related to corrosion charge via Faraday's law. While these tests are indispensable for studying mechanical consequences (cracking, spalling), the corrosion rates and environmental conditions are usually far from service conditions, so direct use of impressed-current parameters in initiation models is not recommended.

7.4.2. Accelerated carbonation in CO_2 chambers

Accelerated carbonation tests expose specimens to elevated CO_2 levels (typically 1–5% by volume) at controlled temperature and humidity, often in specialized carbonation chambers. Carbonation depths are monitored over time and used to back-calculate effective carbonation coefficients. When calibrating models for natural exposure (at $\sim 0.04\%$ CO_2), it is important to account for possible changes in reaction mechanisms and moisture distributions under high CO_2 concentration; direct scaling of coefficients may introduce bias if these effects are neglected.

7.4.3. Temperature and humidity acceleration

Elevated temperature and humidity cycles are sometimes used to accelerate chloride ingress and other transport processes. In the context of the diffusivity models described earlier, such tests can help identify activation energies and humidity-dependence functions, provided that the same constitutive forms (Arrhenius-type temperature dependence, humidity factors) are used to interpret both accelerated and natural-exposure data.

7.5. From Measurements to Model Parameters

The measurements described above enter the modeling workflow through parameter identification and model validation. Simple curve-fitting and more advanced inverse approaches can be used, depending on the richness of the data and the complexity of the model.

7.5.1. Curve fitting and single-test identification

In many applications, apparent diffusion or sorptivity coefficients are obtained by fitting analytical or semi-analytical solutions (e.g., Fickian error-function profiles, $\sqrt{t}$ sorptivity laws) to data from a single test [67]. This approach is straightforward and widely used, but it implicitly absorbs several physical effects (binding, aging, moisture changes) into an effective parameter, which may be specific to the test conditions.

7.5.2. Multi-test and multi-objective calibration

For more mechanistic models, it is advantageous to combine data from several tests—for example, using diffusion/migration tests, sorptivity measurements, and field profiles together—to constrain the same set of parameters. This naturally leads to multi-objective or Bayesian inverse problems, where parameters such as D_{Cl} factors, binding isotherm coefficients, and carbonation-rate constants are adjusted to fit multiple datasets within their experimental uncertainty. Electrochemical measurements (half-cell potentials, polarization resistance, resistivity) can be incorporated as additional constraints on the initiation and corrosion-rate sub-models.

7.5.3. Hybrid physics–data approaches

Hybrid approaches combine physics-based models with data-driven components. Examples include using physics-based transport models to generate features (e.g. predicted C_f and H at the bar depth) that feed into empirical or machine-learning models for i_{corr}, or using data-assimilation techniques to update model states based on monitoring data. Such methods are particularly relevant for long-term monitoring of critical infrastructure, where models must be continually recalibrated as new data arrive.

8. Uncertainty, Variability, and Reliability

A full structural reliability framework for corrosion-affected structures is outside the scope of the present report and is treated separately. Nevertheless, initiation models involve multiple sources of uncertainty and variability that directly affect predicted time-to-initiation and the interpretation of service-life assessment results. This section therefore provides a concise uncertainty and reliability context for corrosion-initiation modeling, rather than a complete reliability methodology.

8.1. Sources and Types of Uncertainty in Initiation Models

Let t_{init} denote the time to depassivation at a given steel location, as predicted by a deterministic model of the form

$$t_{\text{init}} = g(\boldsymbol{\theta}, \mathscr{M}), \tag{88}$$

where $\boldsymbol{\theta}$ collects input parameters (e.g., cover depth, diffusion coefficient, surface concentration, chloride threshold, carbonation rate), and $\mathscr{M}$ denotes the chosen model class (e.g., pure Fickian model, chloride model, carbonation model, or a combined multi-physics formulation). Following common reliability and service life practice [91–93], uncertainties in t_{init} can be grouped as:

- **Parameter variability:** inherent scatter (aleatory) in quantities such as cover depth, concrete diffusivity, humidity exposure, surface chloride concentration, binding capacity, and critical chloride content. For example, cover depth often exhibits significant construction variability, while apparent diffusion coefficients inferred from field profiles scatter over orders of magnitude for nominally similar concretes.
- **Model-form uncertainty:** discrepancies between the chosen model $\mathscr{M}$ and the true physical processes. Examples include the use of one-dimensional diffusion to represent inherently three-dimensional ingress, simplified binding isotherms, empirical humidity factors, and the adoption of a single critical chloride threshold for complex steel–concrete interfaces. Different plausible models (e.g., Fickian vs. multiphase transport; single-ion vs. multi-ion) may yield systematically different t_{init} predictions for the same input data.

- **Measurement and data uncertainty:** noise and bias in laboratory and field measurements used to identify parameters or to define boundary conditions. Examples include scatter in chloride profiles due to sampling and analytical procedures, uncertainty in carbonation depth measurements from phenolphthalein indicators, and noise in electrochemical measurements such as half-cell potentials or polarization resistance [83].

From a practical viewpoint, parameter variability and measurement noise can be quantified and propagated probabilistically once suitable statistical models for $\boldsymbol{\theta}$ and observations are available. Model-form uncertainty is harder to characterize; in many durability studies it is treated implicitly by calibrating model parameters to field data or by comparing predictions from alternative model classes. In formal reliability-based or semi-probabilistic service-life frameworks, the combined effect of parameter uncertainty, model uncertainty, and environmental variability may be represented through characteristic values, partial factors, or target reliability levels [75, 94, 95].

8.2. Role of Corrosion Initiation Models in Service-Life Assessment

In the corrosion-initiation context considered in this report, service-life assessment refers to estimating whether carbonation or chloride ingress is likely to cause reinforcement depassivation before a selected target service life t_d. This use of service life is narrower than life-cycle assessment, which may also consider structural functionality, operational functionality, repair actions, environmental impacts, and end-of-life decisions. Here, the focus is limited to durability-related performance of reinforced concrete components affected by corrosion mechanisms.

Corrosion-initiation models provide the technical link between environmental exposure, material transport properties, depassivation criteria, and the predicted time to initiation. In practice, design codes, standards, guides, and owner requirements may address this problem either indirectly, through prescriptive provisions such as exposure classification, minimum cover, mixture requirements, concrete quality, and protective measures, or more explicitly, through service-life models and reliability-based formats. The basic idea is to assess whether depassivation, or more generally loss of corrosion-related durability performance, is expected to occur before the selected target service life t_d [94, 95].

8.2.1. Durability limit states

At the initiation level, a natural durability limit state is

$$\mathrm{LS}_{\mathrm{init}}: \quad t_{\mathrm{init}} \leq t_d, \tag{89}$$

meaning that depassivation occurs before the design life. Service life design rules can then be interpreted as requirements that the probability of this limit-state event be sufficiently small,

$$\mathbb{P}[t_{\mathrm{init}} \leq t_d] \leq p_{\mathrm{target}}, \tag{90}$$

where p_{target} is a code-specified target probability (or equivalently, a reliability index). In practice, many codes avoid explicit probabilistic language and instead prescribe deterministic rules (minimum cover depths, maximum w/c, concrete quality classes, exposure classes) that are calibrated to approximate Eq. (90) at a system level.

8.2.2. Role of corrosion initiation models in code calibration

Initiation models enter service life design in several ways:

- As *engineering design tools*, where a designer uses an initiation model with conservative parameter values (e.g., characteristic cover depth, upper-bound D_{Cl}, lower-bound C_{crit}) to check that $t_{\text{init}} \geq t_d$ for the selected exposure class.
- As *calibration models*, used by code committees to derive partial factors or prescriptive rules such that the implied distribution of t_{init} across a population of structures achieves a target reliability level. This is the spirit of probabilistic approaches advocated in documents such as the fib Model Code for Service Life Design [75] and the JCSS Probabilistic Model Code [92].
- As *assessment tools* for existing structures, where measured profiles, carbonation depths and electrochemical data are combined with initiation models (possibly in an inverse or Bayesian framework) to estimate residual time to initiation and to inform inspection and maintenance planning.

9. Summary

The physics-based models for corrosion initiation in reinforced concrete are reasonably mature at the level of individual mechanisms (chloride ingress, carbonation, moisture transport), but much less so for their interaction, calibration, and integration with structural performance. This section synthesizes key scientific and modeling gaps and sketches a pragmatic roadmap, with emphasis on multi-physics formulations and data-informed parameterization that can ultimately support reliability-based design and assessment.

9.1. Key Scientific and Modeling Gaps

Considerable progress has been made in understanding and modeling corrosion initiation in reinforced concrete. For many engineering applications, existing models can represent chloride ingress, carbonation advance, moisture-dependent transport, chloride binding, and threshold-based depassivation in a form suitable for service-life assessment. These models are useful for comparing materials, exposure conditions, cover depths, and mitigation strategies, and they provide a practical basis for durability assessment when their assumptions and calibration range are respected.

The remaining gaps should therefore not be interpreted as indicating that corrosion-initiation models are ineffective. Rather, they identify areas where current models are less advanced

when applied to realistic field conditions, spatially heterogeneous materials, combined exposures, localized initiation, and long assessment periods. In this context, the most important scientific and modeling gaps are summarized below:

- **Steel–concrete interface and passive film.** It is well established that the high alkalinity of concrete pore solution promotes steel passivation, and that chloride ingress, carbonation, moisture state, oxygen availability, and local interfacial defects influence depassivation. However, the following issues require further investigation:
  - Limited quantitative models for the ITZ around reinforcement (bleeding, voids, top-bar effects) and its evolution over time.
  - Incomplete mechanistic description of passive-film breakdown and repassivation under realistic pore-solution chemistries.
  - Scarce data linking steel metallurgy, surface condition and micro-structural defects to variability in C_{crit} and initiation modes.
- **Non-uniform and localized initiation.** The importance of localized pitting, macrocell behavior, and spatial variability along reinforcement is well recognized, and simplified stochastic or threshold-based treatments can be used in engineering assessment. However, the following issues require further investigation:
  - Most corrosion initiation models are formulated at a 1D or mean-field level and are not well suited for predicting localized corrosion, including pitting, or macrocell currents along reinforcement, both of which depend on local steel, interface, and exposure conditions.
  - Validated approaches are still needed to represent local extremes, or "weak spots," within continuum-scale initiation models and to relate these localized electrochemical conditions to observable quantities such as half-cell potential, concrete resistivity, local chloride content, and moisture state.
- **Combined actions and multi-ion effects.** Separate models for chloride-induced and carbonation-induced depassivation are well developed, and multi-species transport theory provides a basis for more detailed analysis. However, the following issues require further investigation:
  - Existing practice still often treats chloride-induced and carbonation-induced depassivation separately, with simplified superposition for combined exposures.
  - Multi-ion transport and competitive binding (chloride, hydroxide, carbonate, sulfate) are only partially included in most engineering models, despite clear laboratory evidence of coupled effects.
- **Long-term evolution of transport properties.** Effective diffusion coefficients, carbonation coefficients, moisture-dependent transport functions, and empirical aging

factors provide practical tools for service-life assessment. However, the following issues require further investigation:

  - Time- and damage-dependent changes in diffusivity and permeability (e.g., micro-cracking, leaching, ongoing hydration, SCM reactions) are still represented by crude empirical factors.
  - Limited field-validated models for the joint evolution of transport properties, moisture state and microstructure over decades of exposure.

- **Model-form uncertainty and validation.** Existing models can be calibrated to chloride profiles, carbonation depths, laboratory transport tests, and electrochemical measurements, and they are useful within their calibrated range. However, the following issues require further investigation:
  - Many models are calibrated to narrow datasets and then applied widely, with little quantitative assessment of model-form error.
  - Systematic benchmarks across different codes (FD/FEM/FV, single-ion vs. multi-ion, different binding laws) are rare and often not documented in a way that enables independent replication.

9.2. Data and Calibration Challenges

Robust multi-physics models require data that are often incomplete, inconsistent or not tailored for calibration:

- **Lack of harmonized, multi-modal datasets.**
  - Most studies report either transport data (chloride profiles, carbonation depths) or electrochemical indicators, but rarely both in a coordinated fashion on the same specimens.
  - Micro-structural and chemical characterizations (TGA, XRD, pore structure) are often missing, limiting the ability to constrain reaction and binding sub-models.
- **Inadequate documentation of exposure histories.**
  - Field datasets frequently lack continuous records of humidity, temperature, surface wetting and chloride loading, forcing modelers to rely on idealized boundary conditions.
  - Accelerated tests (migration, high-CO_2, impressed-current) are often reported without sufficient detail to map them rigorously onto service conditions.
- **Transferability from lab to field.**

  - Apparent diffusion coefficients from short-term laboratory tests can differ markedly from effective values inferred from long-term field exposure, with no universally accepted translation framework.
  - Parameters such as C_{crit} and carbonation rate often show strong dependence on specimen geometry, curing and testing protocol, complicating their use in generic models.

- **Statistical characterization and uncertainty quantification.**
  - Many datasets are small and heterogeneous, making it difficult to derive reliable probability distributions and correlation structures for key parameters.
  - Formal treatment of measurement error, censoring (e.g., "no corrosion observed yet"), and model discrepancy remains the exception rather than the rule.

9.3. Integration with Structural Analysis and Multi-Mechanism Aging

Initiation models must be embedded into broader frameworks that capture mechanical consequences and interactions with other degradation mechanisms:

- **Coupling to cracking, bond loss and stiffness degradation.**
  - Need for consistent links between local initiation time, corrosion rate, rust expansion and the evolution of cracking, cover spalling, bond deterioration and stiffness reduction at member level.
  - Integration of corrosion initiation and propagation with nonlinear finite element models for RC members, including appropriate transfer of uncertainties.

- **Interaction with other aging mechanisms.**
  - Corrosion often co-exists with ASR, freeze–thaw, sulfate attack, leaching and mechanical fatigue; joint modeling frameworks are still in their infancy.
  - Moisture and micro-structural states are common drivers for several mechanisms, suggesting opportunities for unified transport and aging models that feed multiple damage processes.

- **From initiation-scale models to system-level reliability.**
  - Translation of initiation-time distributions into durability and structural limit states (and ultimately into risk metrics and decision tools) remains a major research task.
  - Multi-scale frameworks are needed that link material-scale stochastic fields (e.g., $t_{\text{init}}(\mathbf{x})$) to member- and system-level performance, inspection planning and life-cycle optimization.

Overall, this report has aimed to clarify how corrosion initiation in reinforced concrete emerges from the interaction of transport processes, pore solution chemistry, passive-film stability, and environmental exposure. While the underlying mechanisms are complex and span multiple spatial and temporal scales, the review has shown that a coherent hierarchy of models can still be formulated for engineering use, ranging from simplified service-life expressions to more detailed coupled transport frameworks. At the same time, the report has highlighted that reliable prediction depends not only on improved mechanistic descriptions, but also on careful parameterization, calibration against laboratory and field data, and explicit treatment of uncertainty and variability. These considerations motivate continued work toward models that are physically grounded, computationally efficient, and suitable for integration into broader durability, aging, and structural reliability assessments.

References

[1] Qian J, Zhang P, Wu Y, Jia R, Yang J (2024) Study on corrosion monitoring of reinforced concrete based on longitudinal guided ultrasonic waves. *Applied Sciences* 14(3):1201.

[2] National Institute of Standards and Technology (2017) Move over, Superman: NIST 'spectral fingerprinting' sees through concrete to spot corrosion, NIST News Release. Accessed 19 November 2025 Available at https://www.nist.gov/news-events/news/2017/04/move-over-superman-nist-spectral-fingerprinting-sees-through-concrete-0.

[3] Tuutti K (1982) Corrosion of steel in concrete .

[4] Angst UM (2018) Challenges and opportunities in corrosion of steel in concrete. *Materials and Structures* 51(1):4.

[5] Rodrigues R, Gaboreau S, Gance J, Ignatiadis I, Betelu S (2021) Reinforced concrete structures: A review of corrosion mechanisms and advances in electrical methods for corrosion monitoring. *Construction and Building Materials* 269:121240.

[6] Angst UM, Polder R (2014) Spatial variability of chloride in concrete within homogeneously exposed areas. *Cement and Concrete Research* 56:40–51.

[7] Pourbaix M (1966) Atlas of electrochemical equilibria in aqueous solutions. *NACE* .

[8] Angst U, Rønnquist A, Elsener B, Larsen CK, Vennesland Ø (2011) Probabilistic considerations on the effect of specimen size on the critical chloride content in reinforced concrete. *Corrosion Science* 53(1):177–187.

[9] Angst UM (2019) Predicting the time to corrosion initiation in reinforced concrete structures exposed to chlorides. *Cement and Concrete Research* 115:559–567.

[10] Poursaee A, Angst UM (2023) Principles of corrosion of steel in concrete structures. *Corrosion of steel in concrete structures* (Elsevier), pp 17–34.

[11] Tuutti K (1980) Service life of structures with regard to corrosion of embedded steel. *Special Publication* 65:223–236.

[12] Biczok I, Blasovszky N (1964) *Concrete corrosion and concrete protection* (Akademiai Kiado Budapest, Hungary).

[13] Taylor HF (1997) *Cement chemistry* (Thomas Telford).

[14] Scrivener KL, Nonat A (2011) Hydration of cementitious materials, present and future. *Cement and concrete research* 41(7):651–665.

[15] Mehta PK, Monteiro PJ (2006) *Concrete microstructure, properties, and materials* (McGraw-hill).

[16] Diamond S (2004) The microstructure of cement paste and concrete—-a visual primer. *Cement and concrete composites* 26(8):919–933.

[17] Patel RA, Phung QT, Seetharam SC, Perko J, Jacques D, Maes N, De Schutter G, Ye G, Van Breugel K (2016) Diffusivity of saturated ordinary portland cement-based materials: A critical review of experimental and analytical modelling approaches. *Cement and Concrete Research* 90:52–72.

[18] Walker CS, Sutou S, Oda C, Mihara M, Honda A (2016) Calcium silicate hydrate (csh) gel solubility data and a discrete solid phase model at 25 c based on two binary

non-ideal solid solutions. *Cement and Concrete Research* 79:1–30.

[19] Bentz DP, Garboczi EJ (1991) Percolation of phases in a three-dimensional cement paste microstructural model. *Cement and concrete research* 21(2-3):325–344.

[20] von Greve-Dierfeld S, Lothenbach B, Vollpracht A, Wu B, Huet B, Andrade C, Medina C, Thiel C, Gruyaert E, Vanoutrive H, et al. (2020) Understanding the carbonation of concrete with supplementary cementitious materials: a critical review by rilem tc 281-ccc. *Materials and structures* 53(6):136.

[21] Scrivener KL, Crumbie AK, Laugesen P (2004) The interfacial transition zone (itz) between cement paste and aggregate in concrete. *Interface science* 12(4):411–421.

[22] Angst U, Elsener B, Larsen CK, Vennesland Ø (2009) Critical chloride content in reinforced concrete—a review. *Cement and concrete research* 39(12):1122–1138.

[23] Yang H, Che Y, Leng F (2018) Calcium leaching behavior of cementitious materials in hydrochloric acid solution. *Scientific reports* 8(1):8806.

[24] Luping T, Nilsson LO (1993) Chloride binding capacity and binding isotherms of opc pastes and mortars. *Cement and concrete research* 23(2):247–253.

[25] Scrivener KL (2004) Backscattered electron imaging of cementitious microstructures: understanding and quantification. *Cement and concrete Composites* 26(8):935–945.

[26] Elsharief A, Cohen MD, Olek J (2003) Influence of aggregate size, water cement ratio and age on the microstructure of the interfacial transition zone. *Cement and concrete research* 33(11):1837–1849.

[27] Zhang Z, Angst U, Michel A, Jensen MA (2018) An image-based local homogenization method to model mass transport at the steel-concrete interface. *Sixth International Conference on Durability of Concrete Structures ICDCS 2018* (Whittles Publishing), pp 807–814.

[28] Bentz D, Hwang J, Hagwood C, Garboczi E, Snyder K, Buenfeld N, Scrivener K (1994) Interfacial zone percolation in concrete: Effects of interfacial zone thickness and aggregate shape. *MRS Online Proceedings Library (OPL)* 370:437.

[29] Garboczi EJ, Bentz DP (1997) Analytical formulas for interfacial transition zone properties. *Advanced Cement Based Materials* 6(3-4):99–108.

[30] Zhang Z, Angst U, Michel A (2018) A framework for modelling corrosion-related degradation in reinforced concrete. *IALCCE* :979–986.

[31] Garboczi EJ, Bentz DP (1998) Multiscale analytical/numerical theory of the diffusivity of concrete. *Advanced Cement Based Materials* 8(2):77–88.

[32] Snyder KA (2001) The relationship between the formation factor and the diffusion coefficient of porous materials saturated with concentrated electrolytes: theoretical and experimental considerations. *Concrete Science and Engineering* 3(12):216–224.

[33] Snyder KA, Marchand J (2001) Effect of speciation on the apparent diffusion coefficient in nonreactive porous systems. *Cement and Concrete Research* 31(12):1837–1845.

[34] Linderoth O, Johansson P, Wadsö L (2020) Development of pore structure, moisture sorption and transport properties in fly ash blended cement-based materials. *Construction and Building Materials* 261:120007.

[35] Dhandapani Y, Santhanam M (2017) Assessment of pore structure evolution in the limestone calcined clay cementitious system and its implications for performance. *Cement and Concrete Composites* 84:36–47.
[36] Šavija B, Luković M (2016) Carbonation of cement paste: Understanding, challenges, and opportunities. *Construction and Building Materials* 117:285–301.
[37] Marchand J (2001) Modeling the behavior of unsaturated cement systems exposed to aggressive chemical environments. *Materials and structures* 34(4):195–200.
[38] Samson E, Marchand J, Snyder KA, Beaudoin J (2005) Modeling ion and fluid transport in unsaturated cement systems in isothermal conditions. *Cement and Concrete Research* 35(1):141–153.
[39] Samson E, Marchand J (2007) Modeling the transport of ions in unsaturated cement-based materials. *Computers & Structures* 85(23-24):1740–1756.
[40] Bishnoi S, Bullard JW (2021) Microstructure models of cement: their importance, utility, and current limitations. *RILEM Technical Letters* 6:188–195.
[41] Goyal A, Pouya HS, Ganjian E, Claisse P (2018) A review of corrosion and protection of steel in concrete. *Arabian Journal for Science and Engineering* 43(10):5035–5055.
[42] Volokitina I, Volokitin A, Panin E (2024) Gradient microstructure formation in carbon steel bars. *Journal of Materials Research and Technology* 31:2985–2993.
[43] Katiyar PK, Maurya R, Singh PK (2022) Corrosion behavior of plain carbon steels under different heat treatment conditions in freely aerated 3.5% nacl solution. *International Journal of Sustainable Building Technology and Urban Development* 13(1):44–68.
[44] Angst UM, Geiker MR, Michel A, Gehlen C, Wong H, Isgor OB, Elsener B, Hansson CM, François R, Hornbostel K, et al. (2017) The steel–concrete interface. *Materials and Structures* 50(2):143.
[45] Wong HS, Angst UM, Geiker MR, Isgor OB, Elsener B, Michel A, Alonso MC, Correia MJ, Pacheco J, Gulikers J, et al. (2022) Methods for characterising the steel–concrete interface to enhance understanding of reinforcement corrosion: a critical review by rilem tc 262-sci. *Materials and structures* 55(4):124.
[46] Lv S, Li K (2022) Semiconducting behaviour and corrosion resistance of passive film on corrosion-resistant steel rebars. *Materials* 15(21):7644.
[47] Wang X, Yu X, Jin M, Zhou Y, Liu J (2024) Cations effect on the passive film for carbon steels in concrete simulated pore solutions. *Journal of Building Engineering* 94:109945.
[48] Popov BN (2015) *Corrosion engineering: principles and solved problems* (Elsevier).
[49] Glass G, Buenfeld N (2000) Chloride-induced corrosion of steel in concrete. *Progress in Structural Engineering and Materials* 2(4):448–458.
[50] Bertolini L, Elsener B, Pedeferri P, Redaelli E, Polder RB (2013) *Corrosion of steel in concrete: prevention, diagnosis, repair* (John Wiley & Sons).
[51] Angst U, Moro F, Geiker M, Kessler S, Beushausen H, Andrade C, Lahdensivu J, Köliö A, Imamoto Ki, von Greve-Dierfeld S, et al. (2020) Corrosion of steel in carbonated concrete: mechanisms, practical experience, and research priorities–a critical

review by rilem tc 281-ccc. *RILEM technical letters* 5:85–100.

[52] Broomfield JP (2023) *Corrosion of steel in concrete: understanding, investigation and repair* (Crc Press).

[53] Jamali A, Angst U, Adey B, Elsener B (2013) Modeling of corrosion-induced concrete cover cracking: A critical analysis. *Construction and Building Materials* 42:225–237.

[54] Morinaga S (1988) Prediction of service lives of reinforced concrete buildings based on rate of corrosion of reinforcing steel. *Special report of institute of technology, Shimizu corporation* 23.

[55] Andrade C, Alonso C, Molina F (1993) Cover cracking as a function of bar corrosion: Part i-experimental test. *Materials and structures* 26(8):453–464.

[56] Purvis RL, Babaei K, Clear K, Markow M (1994) Life-cycle cost analysis for protection and rehabilitation of concrete bridges relative to reinforcement corrosion. *Contract* 100:104.

[57] Rodriguez J, Ortega L, Casal J, Diez J (2018) Corrosion of reinforcement and service life of concrete structures. *Durability of Building Materials & Components 7 vol. 1* (Routledge), pp 117–126.

[58] DuraCrete (1998) Modeling of degradation (BRITE-EURAM Project BE95-1347, Gouda, The Netherlands), Report R4-5.

[59] Alonso C, Andrade C, Rodriguez J, Diez JM (1998) Factors controlling cracking of concrete affected by reinforcement corrosion. *Materials and structures* 31(7):435–441.

[60] Webster MP (2000) *The assessment of corrosion-damaged concrete structures*. Ph.D. thesis. University of Birmingham, .

[61] Torres-Acosta AA, Sagues AA (2004) Concrete cracking by localized steel corrosion–geometric effects. *Materials Journal* 101(6):501–507.

[62] Bažant ZP (1979) Physical model for steel corrosion in concrete sea structures—application. *Journal of the structural division* 105(6):1155–1166.

[63] El Maaddawy T, Soudki K (2007) A model for prediction of time from corrosion initiation to corrosion cracking. *Cement and concrete composites* 29(3):168–175.

[64] Lu C, Jin W, Liu R (2011) Reinforcement corrosion-induced cover cracking and its time prediction for reinforced concrete structures. *Corrosion Science* 53(4):1337–1347.

[65] Winslow DN, Cohen MD, Bentz DP, Snyder KA, Garboczi EJ (1994) Percolation and pore structure in mortars and concrete. *Cement and concrete research* 24(1):25–37.

[66] Baroghel-Bouny V, Wang X, Thiery M, Saillio M, Barberon F (2012) Prediction of chloride binding isotherms of cementitious materials by analytical model or numerical inverse analysis. *Cement and concrete research* 42(9):1207–1224.

[67] Crank J (1979) *The mathematics of diffusion* (Oxford university press).

[68] De Weerdt K, Wilson W, Machner A, Georget F (2023) Chloride profiles–what do they tell us and how should they be used? *Cement and Concrete Research* 173:107287.

[69] Alsheet F, Razaqpur AG, Kim Y (2022) Influence of chloride transport modes and hydrated cement chemistry on chloride profile and binding mechanisms in concrete. *Journal of Materials in Civil Engineering* 34(12):04022351.
[70] Papadakis VG, Vayenas CG, Fardis MN (1991) Fundamental modeling and experimental investigation of concrete carbonation. *Materials Journal* 88(4):363–373.
[71] Saetta AV, Schrefler BA, Vitaliani RV (1995) 2—d model for carbonation and moisture/heat flow in porous materials. *Cement and Concrete research* 25(8):1703–1712.
[72] Ngo VD, Nguyen NT, Duprat F, Vu NT, Nguyen VP (2021) Climatic issue in an advanced numerical modeling of concrete carbonation. *Sustainability* 13(11):5994.
[73] Li D, Li Ly, Wang X (2020) Mathematical modelling of concrete carbonation with moving boundary. *International Communications in Heat and Mass Transfer* 117:104809.
[74] Thomas M (2013) *Supplementary cementing materials in concrete* (CRC press).
[75] Fédération internationale du béton (fib) Task Group 101 (2024) *fib Model Code for Concrete Structures (2020)* (International Federation for Structural Concrete (fib)), version 1.2 Ed. Fib Bulletin No. 2020.
[76] Lee JM, Hong SI, Yang HJ, Jung DH (2022) Numerical modeling of chloride transport in concrete under cyclic exposure to chloride. *Materials* 15(17):5966.
[77] Saouma V, Hariri-Ardebili M (2021) *Aging, Shaking, and Cracking of Infrastructures: From Mechanics to Concrete Dams and Nuclear Structures* (Springer).
[78] Xi Y, Bažant ZP (1999) Modeling chloride penetration in saturated concrete. *Journal of Materials in Civil Engineering* 11(1):58–65.
[79] Saetta AV, Schrefler BA, Vitaliani RV (1993) The carbonation of concrete and the mechanism of moisture, heat and carbon dioxide flow through porous materials. *Cement and Concrete Research* 23(4):761–772.
[80] Ababneh A, Benboudjema F, Xi Y (2003) Chloride penetration in nonsaturated concrete. *Journal of materials in civil engineering* 15(2):183–191.
[81] Newman J, Thomas-Alyea KE (2012) *Electrochemical systems* (John Wiley & Sons).
[82] Jones DA (1996) Principles and prevention of corrosion. *(No Title)* .
[83] Andrade C, Alonso C (2001) On-site measurements of corrosion rate of reinforcements. *Construction and building materials* 15(2-3):141–145.
[84] ASTM International (2011) Astm c1556: Standard test method for determining the apparent chloride diffusion coefficient of cementitious mixtures by bulk diffusion, Standard C1556, ASTM International, West Conshohocken, PA.
[85] ASTM International (2012) Astm c1202: Standard test method for electrical indication of concrete's ability to resist chloride ion penetration, Standard C1202, ASTM International, West Conshohocken, PA.
[86] ASTM International (2013) Astm c1585: Standard test method for measurement of rate of absorption of water by hydraulic-cement concretes, Standard C1585, ASTM International, West Conshohocken, PA.
[87] ASTM International (2012) Astm c1152: Standard test method for acid-soluble chloride in mortar and concrete, Standard C1152, ASTM International, West Con-

shohocken, PA.

[88] ASTM International (2009) Astm c876: Standard test method for corrosion potentials of uncoated reinforcing steel in concrete, Standard C876, ASTM International, West Conshohocken, PA.

[89] Stern M, Geary AL (1957) Electrochemical polarization: I. a theoretical analysis of the shape of polarization curves. *Journal of the electrochemical society* 104(1):56.

[90] Orazem ME, Tribollet B (2008) Electrochemical impedance spectroscopy. *New Jersey* 1(906):383–389.

[91] Vu KAT, Stewart MG (2000) Structural reliability of concrete bridges including improved chloride-induced corrosion models. *Structural safety* 22(4):313–333.

[92] Vrouwenvelder T, et al. (1997) The jcss probabilistic model code. *Structural Safety* 19(3):245–251.

[93] Violetta B (2002) Life-365 service life prediction model. *Concrete international* 24(12):53–57.

[94] Saassouh B, Lounis Z (2012) Probabilistic modeling of chloride-induced corrosion in concrete structures using first-and second-order reliability methods. *Cement and Concrete Composites* 34(9):1082–1093.

[95] Hamidane H, Chateauneuf A, Messabhia A, Ababneh A (2020) Reliability analysis of corrosion initiation in reinforced concrete structures subjected to chlorides in presence of epistemic uncertainties. *Structural Safety* 86:101976.